MOX-Report No. 17/2022

Stabilization of staggered time discretization schemes for 0D-3D fluid-structure interaction problems

Regazzoni, F.

MOX, Dipartimento di Matematica
Politecnico di Milano, Via Bonardi 9 - 20133 Milano (Italy)

mox-dmat@polimi.it http://mox.polimi.it

Stabilization of staggered time discretization schemes for 0D-3D fluid-structure interaction problems

F. Regazzoni[1]

[1]MOX - Dipartimento di Matematica, Politecnico di Milano,
P.zza Leonardo da Vinci 32, 20133 Milano, Italy
francesco.regazzoni@polimi.it

Abstract

In this paper we analyze the numerical oscillations affecting time-staggered schemes for 0D-3D fluid-structure interaction (FSI) problems, which arise e.g. in the field of cardiovascular modeling, and we propose a novel stabilized scheme that cures this issue. We study two staggered schemes. In the first one, the 0D fluid model prescribes the pressure to the 3D structural mechanics model and receives the flow. In the second one, on the contrary, the fluid model receives the pressure and prescribes the flow. These schemes are respectively known, in the FSI literature, as Dirichlet-Neumann and Neumann-Dirichlet schemes, borrowing these terms from domain decomposition methods, although here a single iteration is performed before moving on to the next time step. Should the fluid be enclosed in a cavity, the Dirichlet-Neumann scheme is affected by non-physical oscillations whose origin lies in the balloon dilemma, for which we provide an algebraic interpretation. Moreover, we show that also the Neumann-Dirichlet scheme can be unstable for a range of parameter choices. Surprisingly, increasing either the viscous dissipation or the inertia of the structure favours the onset of oscillations. Our analysis provides an explanation for this fact and yields sharp stability bounds on the time step size. Inspired by physical considerations on the onset of oscillations, we propose a numerically consistent stabilization term for the Neumann-Dirichlet scheme. We prove that our proposed stabilized scheme is absolutely stable for any choice of time step size. These results are verified by several numerical tests. Finally, we apply the proposed stabilized scheme to an important problem in cardiac electromechanics, namely the coupling between a 3D model and a closed-loop lumped-parameter model of blood circulation. In this setting, our proposed scheme successfully removes the non-physical oscillations that would otherwise affect the numerical solution.

Keywords Fluid-structure interaction, Time-staggered schemes, Numerical stability, Multiscale models, Cardiovascular simulations

MSC Classification 65N

1 Introduction

The numerical solution of fluid-structure interaction (FSI) problems presents many challenges [2, 14, 31, 48]. Numerical instabilities often accompany time-staggered schemes, which alternate the solution of fluid and solid subproblems [11, 15, 17, 24]. The numerical stability of these schemes has been investigated in [8] and in subsequent works [4, 13, 16, 28]. In these research works, however, either the flow rate of the incoming fluid or its pressure is considered to be assigned. This framework therefore does not include cases of practical interest, such as the interaction between a cardiac chamber and blood. In this case, in fact, the blood flow entering and leaving the chamber is not known *a priori*, but should be related to the blood pressure by means of a suitable mathematical model describing the dynamics of the heart valves [23, 43] (see Fig. 1). This can lead to numerical instabilities when using staggered schemes. As a matter of fact, non-physical oscillations may occur even with simplified fluid models, such as 0D models (lumped-parameter models) and by neglecting fluid inertia [3, 23, 32, 43]. These issues are still not well

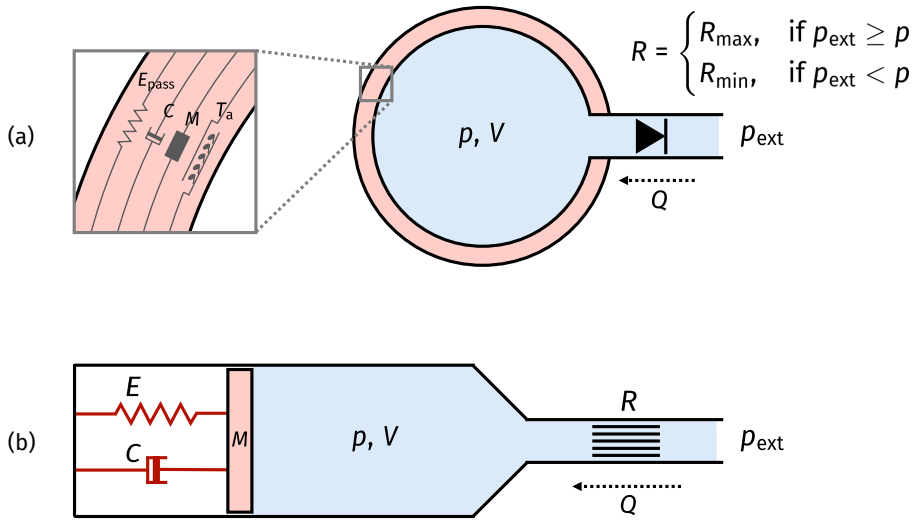

Figure 1: Representation of two model problems that fall within the scope of this paper. The problem (a) consists of a cardiac chamber, represented as an idealized spherical cavity (in red), interacting with blood (in blue), whose state is characterized by the pressure p and the volume V. The dynamics of the chamber accounts for stiffness (E_{pass}), inertia (M), viscosity (C) and the presence of an active tension (T_{a}). The chamber is connected to an external region of pressure p_{ext} through a valve, characterized by a blood flow resistance R, which is very large when $p_{\text{ext}} \geq p$ (closed valve), very small when $p_{\text{ext}} < p$ (open valve). As we will show, this problem can be formally reduced to the piston problem (b), in which a fluid exerts a pressure p against a piston characterized by stiffness (E), inertia (M) and viscous damping (C). The fluid flow is determined as $Q = (p_{\text{ext}} - p)/R$, where R is the fluid flow resistance. More details will be provided below.

understood, and, to the best of our knowledge, to date there is no mathematical explanation for the onset of oscillations and no estimates that can predict for which parameter values and time step sizes they occur. Moreover, the only known cure to date is to use monolithic schemes (that is, solving the coupled problem in one shot) instead of staggered ones.

In this paper we analyze and propose a cure for these numerical oscillations. To this end, we consider the cardiac case as a model problem with a great applicative interest. This test case comprises several features that are challenging from the numerical standpoint. Indeed, when the heart valves are closed (during the so-called isovolumetric phases of the heartbeat), the problem translates into that of an incompressible fluid enclosed in a cavity. Instead, when the outflow valves open, we have a rapid flow ejection. Furthermore, this problem presents some peculiarities, related to the fact that the structure does not move in a purely passive way, but might present an active stress. This, as we shall see, has implications for numerical stability, and can be a further cause of non-physical oscillations. As for the fluid, we will limit ourselves to a 0D description, which is typically adopted for simulations of cardiac electromechanics [3, 23, 32, 43], and which in itself poses a wide range of numerical challenges.

At the continuous level, the 3D structure model and the 0D fluid model are coupled by imposing the continuity of fluxes and pressures [35, 43]. At the numerical level, instead, several coupling schemes between the 3D and the 0D sub-models are possible. An approach is to solve them simultaneously, as a single monolithic system, by means, e.g., of a Newton nonlinear solver [23]. This requires at each iteration the calculation of the Jacobian matrix, which contains the derivatives of the residual with respect to the unknowns. However, assembling the blocks of the Jacobian matrix associated with the fluid model might involve a significant implementation effort, especially for fluid models with a large number of unknowns (see e.g. [1, 43]). An attractive alternative to monolithic schemes is represented by staggered schemes (in some contexts called partitioned schemes), that alternate the solution of the fluid model and of the structure mechanics model. This allows for a much easier implementation than monolithic schemes and yields the possibility to reuse pre-existing (even black-box) solvers for either the 3D structure model or

the 0D fluid model. However, as mentioned, staggered schemes may suffer from numerical instability, which is manifested in non-physical oscillations in the solution.

In this paper we will focus on two staggered schemes. Within the first one, the structural model provides the flows and receives the pressures from the fluid model; within the second scheme, instead, the structural model provides the pressures and receives the flows. These schemes are known in the literature, respectively, as Dirichlet-Neumann and Neumann-Dirichlet scheme [4, 8, 24, 28]. These names are borrowed, with a little abuse of notation, from the field of domain decomposition methods (see e.g. [38, 50]). However, it is important to note that, while in domain decomposition methods one iterates between the two models until convergence, with time-staggered schemes one advances to the next time step after a single iteration between the two models. Although with a 0D fluid there is no physical boundary, we will use the terms Dirichlet-Neumann and Neumann-Dirichlet by analogy to the 3D case. Indeed, in the 0D case, the Dirichlet condition translates into imposing fluid flow, while the Neumann condition into imposing pressure.

Although the Dirichlet-Neumann scheme requires a simpler implementation than Neumann-Dirichlet's (pressures are assigned as boundary conditions to the structure mechanics model and fluxes are post-processed from the displacement), it is characterized by serious numerical instability issues when an incompressible fluid is enclosed in a cavity (this is the case, e.g., of isovolumetric phases of the heartbeat [25]). This issue, known as balloon dilemma, is explained by the impossibility to satisfy the incompressibility constraint of the fluid contained in the cavity if the pressure is assigned [5, 20]. As a workaround, it is possible to iterate the resolution of the structure mechanics problem, updating the pressure based on an estimate of the cavity compliance (i.e. $\partial V/\partial p$, where p and V are the cavity pressure and volume, respectively), in order to satisfy the volumetric constraint [18, 25]. However, a poorly accurate estimate of the compliance could lead to a very slow convergence or even to failure of the solver.

To avoid the balloon dilemma, the pressures acting inside the cavities should not be decoupled from the displacement. This requirement can be accommodated in the framework of the Neumann-Dirichlet staggered approach, in which the structure mechanics model is solved under the constraint that the volume contained in the cavity coincides with that predicted, at the previous iteration, by the fluid model. Then, the obtained pressure is provided to the fluid model, to advance to the next time iteration. The pressure in the cavity can be interpreted in this context as a Lagrange multiplier that ensures that the volume constraint is satisfied [3, 35, 43].

The Neumann-Dirichlet scheme solves the balloon dilemma and prevents the spurious oscillations that would otherwise occur for cavity problems when using the Dirichlet-Neumann scheme. However, it is possible that in presence of a rapid fluid flow (e.g. in cardiac case, when at least one valve is open) non-physical oscillations still occur, even when using the Neumann-Dirichlet scheme. In Fig. 2 we display an example of oscillations obtained when applying the Neumann-Dirichlet scheme to a multiscale model of cardiac electromechanics of the left ventricle (the model is described in detail in Sec 5.2). As we will show, these oscillations may depend on the time step used, on the model parameters (in particular the stiffness, viscosity and inertia associated with the structure) and on the force generation model in use.

As mentioned, this paper has a twofold objective. On the one hand, it aims to provide a theoretical basis that explains the occurrence of these oscillatory phenomena and that can predict for which parameter values and for which time step range the numerical scheme is stable. On the other hand, it proposes a stabilized scheme that cures these non-physical oscillations, while retaining the advantages of staggered schemes.

The paper is organized as follows. First, in Sec. 2, we introduce the mathematical models and the numerical schemes considered in this paper. Then, in Sec. 3 we study the numerical stability of the schemes introduced above. In Sec. 4 we propose a cure for the observed instability issues, by means of the introduction of a numerically consistent stability term. Then, in Sec. 5, we present and discuss several numerical results obtained, on the one hand, with a model FSI problem and, on the other hand, with a multiscale and multiphysics model of cardiac electromechanics. Finally, we draw our conclusions and final remarks in Sec. 6.

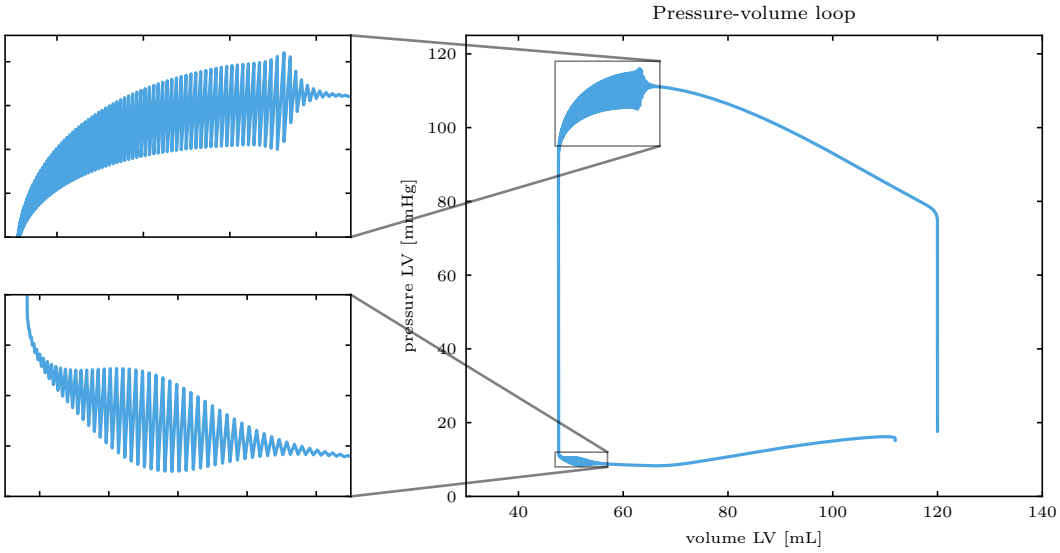

Figure 2: Non-physical oscillations, obtained when employing the Neumann-Dirichlet scheme to numerically approximate the left ventricle model of cardiac electromechanics described in Sec 5.2. The graph shows the simulation results in the pressure-volume phase plane. The onset of oscillations is shown in two enlargements (left).

2 Mathematical models and numerical schemes

In this section we introduce a generic model of cardiac mechanics and blood dynamics, encompassing many of the models available in the literature [3, 23, 32, 43] and the associated numerical schemes that will be addressed in the sequel of this paper.

2.1 Mathematical models

We consider a computational domain Ω_0, representing the region of space occupied by the muscle tissue at rest (see Fig. 3). The domain Ω_0 can represent a 4-chamber whole heart, or a part of it, composed of $N < 4$ chambers. To each point of Ω_0, we associate a unit vector $\mathbf{f}_0$, denoting the local direction of cardiac fibers. Let us denote by $\mathbf{d}(\mathbf{x}, t)$ the displacement of the material point $\mathbf{x}$ at time t (we have $\mathbf{d}\colon \Omega_0 \times [0, +\infty) \to \mathbb{R}^3$). We then introduce the variables $p_1(t), p_2(t), \ldots, p_N(t)$, which represent the (constant in space) blood pressures contained in the N heart chambers. Similarly, we denote by $\Gamma_0^{\text{endo,i}} \subset \partial\Omega_0$, for $i = 1, \ldots, N$, the domain boundary associated with the i-th chamber (endocardial cavity). Since the cardiac tissue is an active material, we denote by $T_\text{a}(\mathbf{x}, t)$ the local active tension that acts in the fiber direction. The active tension can be *a priori* imposed [3], or provided by means of a suitable cardiomyocyte model [30, 41, 47]. Finally, to model the passive mechanical behavior of the tissue, we consider an hyperelastic model, associated with the strain energy density functional $\mathcal{W}$. Hence, the Piola-Kirchhoff stress tensor reads

$$\mathbf{P}(\mathbf{d}, T_\text{a}) = \frac{\partial \mathcal{W}(\mathbf{F})}{\partial \mathbf{F}} + T_\text{a} \frac{\mathbf{F}\mathbf{f}_0 \otimes \mathbf{f}_0}{\sqrt{\mathcal{I}_{4f}}}, \tag{1}$$

where the invariant $\mathcal{I}_{4f} = \mathbf{F}\mathbf{f}_0 \cdot \mathbf{F}\mathbf{f}_0$ is a measure of the tissue stretch along the fiber direction. In conclusion, the dynamics of the displacement field $\mathbf{d}$ is described by the following equation, expressing

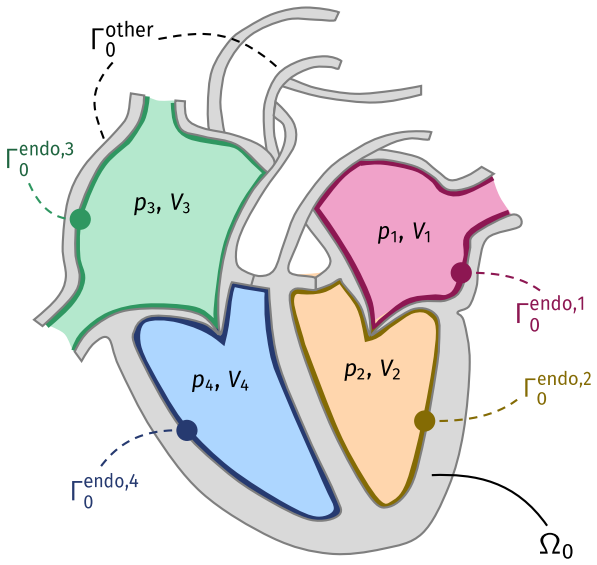

Figure 3: Representation of the domain and boundary conditions of problem (2) with four cavities ($N = 4$), corresponding to the two atria and the two ventricles.

the balance of momentum for the continuum [34]:

$$\begin{cases} \rho \dfrac{\partial^2 \mathbf{d}}{\partial t^2} - \nabla \cdot \mathbf{P}(\mathbf{d}, T_a) = \mathbf{0}, & \text{in } \Omega_0 \times (0, +\infty), \\ \mathbf{P}(\mathbf{d}, T_a)\mathbf{N} = -p_i \, J\mathbf{F}^{-T}\mathbf{N} & \text{on } \Gamma_0^{endo,i} \times (0, +\infty), \text{ for } i = 1, \dots, N, \\ + \textit{ boundary conditions} & \text{on } \Gamma_0^{other} \times (0, +\infty), \\ \mathbf{d} = \mathbf{d}_0, \ \dfrac{\partial \mathbf{d}}{\partial t} = \mathbf{0}, & \text{in } \Omega_0 \times \{0\}, \end{cases} \tag{2}$$

where $\mathbf{N}$ denotes the outer unit normal vector and where suitable boundary conditions are assigned on the remaining portion of the boundary $\Gamma_0^{other} = \partial\Omega_0 \setminus \bigcup_{i=1}^{N} \Gamma_0^{endo,i}$. Typically, spring-dashpot boundary conditions are considered, to account for the presence of the pericardium (see e.g. [43, 52]).

For the sake of brevity, in what follows we will write Eq. (2) in the following compact form, by denoting by $\mathbf{p}(t) = (p_1(t), p_2(t), \dots, p_N(t))$ the vector of the N pressures:

$$\begin{cases} \mathcal{L}(\ddot{\mathbf{d}}(t), \dot{\mathbf{d}}(t), \mathbf{d}(t), \mathbf{p}(t), t) = 0 & t > 0, \\ \mathbf{d}(0) = \mathbf{d}_0, \ \dot{\mathbf{d}}(0) = \mathbf{0}, \end{cases} \tag{3}$$

In the structure mechanics model (3), henceforth called model $\mathcal{S}$, by $\mathcal{L}$ we denote a differential operator that encodes both the PDE and the the associated boundary conditions. Moreover, $\dot{\mathbf{d}}$ and $\ddot{\mathbf{d}}$ denote the first and second time derivatives. These terms are associated with viscosity and inertia, respectively. In particular, viscous effects can be due either to the boundary conditions or to a viscoelastic model used in replacement of the hyperelastic model of Eq. (1). Some authors neglect these terms, i.e. consider a quasi-static formulation, which can be obtained as a special case of (3) [37]. In what follows we will investigate the effects of neglecting inertia, viscosity or both in the structure mechanics model, in terms of numerical stability of the discrete scheme.

To close the model $\mathcal{S}$, we couple it with a lumped-parameter model of fluid dynamics (denoted as model $\mathcal{F}$), describing the vessels surrounding the heart, or even the whole circulatory system. We consider an ODE model in the form of

$$\begin{cases} \dot{\mathbf{c}}(t) = \mathbf{H}(\mathbf{c}(t), \mathbf{p}(t), t) & t > 0, \\ \mathbf{c}(0) = \mathbf{c}_0, \end{cases} \tag{4}$$

where $\mathbf{c}(t)$ is the state vector of the model $\mathcal{F}$ (including pressures, volume and fluxes of the circulatory compartments represented within the model). For concrete examples of (4), see [7, 23, 43].

To couple the models $\mathcal{S}$ and $\mathcal{F}$, we consider the following pairing condition, that enforces the correspondence of the cardiac chamber volumes represented within the two models:

$$\mathbf{V}_{\mathcal{S}}(\mathbf{d}(t)) = \mathbf{V}_{\mathcal{F}}(\mathbf{c}(t)) \qquad t > 0, \tag{5}$$

where $\mathbf{V}_{\mathcal{S}} = (V_{\mathcal{S}}^1, V_{\mathcal{S}}^2, \dots, V_{\mathcal{S}}^N)$ and $\mathbf{V}_{\mathcal{F}} = (V_{\mathcal{F}}^1, V_{\mathcal{F}}^2, \dots, V_{\mathcal{F}}^N)$ are two vectors collecting the blood volumes associate with the N cardiac chambers, as predicted by the $\mathcal{S}$ and $\mathcal{F}$ models respectively. Hence, the coupled FSI model $\mathcal{F}$–$\mathcal{S}$ reads

$$\begin{cases} \mathcal{L}(\ddot{\mathbf{d}}(t), \dot{\mathbf{d}}(t), \mathbf{d}(t), \mathbf{p}(t), t) = 0 & t > 0, \\ \dot{\mathbf{c}}(t) = \mathbf{H}(\mathbf{c}(t), \mathbf{p}(t), t) & t > 0, \\ \mathbf{V}_{\mathcal{S}}(\mathbf{d}(t)) = \mathbf{V}_{\mathcal{F}}(\mathbf{c}(t)) & t > 0, \\ \mathbf{d}(0) = \mathbf{d}_0,\ \dot{\mathbf{d}}(0) = \mathbf{0},\ \mathbf{c}(0) = \mathbf{c}_0. \end{cases} \tag{6}$$

We remark that the blood pressures $\mathbf{p}(t)$ can be interpreted in this context as Lagrange multipliers that enforce the volume compatibility between the models $\mathcal{S}$ and $\mathcal{F}$ at each time $t > 0$.

2.2 Numerical schemes

We now deal with the numerical approximation of the FSI model $\mathcal{F}$–$\mathcal{S}$. Since our goal is to investigate the numerical stability properties of the time discretization scheme, we do not focus on any particular space discretization technique. For example, we observe that Eq. (6) can be interpreted as a system of ODEs resulting from the semi-discretization in space of the continuous model, using, e.g., the Finite Element Method [10]. Furthermore, for simplicity, we consider a first-order finite difference scheme to advance the individual models in time.

We consider a uniform sampling of the time interval with time step $\Delta t > 0$. Specifically, we define $t_k = k\,\Delta t$, and we denote with superscript (k) the approximation of a given variable at the k-th time iteration (e.g., we have $\mathbf{d}^{(k)} \approx \mathbf{d}(t_k)$).

Monolithic scheme

One solution approach is to address at each time step the monolithic system:

$$\begin{cases} \mathcal{L}\left(\dfrac{\mathbf{d}^{(k+1)} - 2\mathbf{d}^{(k)} + \mathbf{d}^{(k-1)}}{\Delta t^2}, \dfrac{\mathbf{d}^{(k+1)} - \mathbf{d}^{(k)}}{\Delta t}, \mathbf{d}^{(k+1)}, \mathbf{p}^{(k+1)}, t_{k+1}\right) = 0 & k = 0, 1, \dots \\ \dfrac{\mathbf{c}^{(k+1)} - \mathbf{c}^{(k)}}{\Delta t} = \mathbf{H}\left(\mathbf{c}^{(\star)}, \mathbf{p}^{(k+1)}, t_{k+1}\right) & k = 0, 1, \dots \\ \mathbf{V}_{\mathcal{S}}(\mathbf{d}^{(k+1)}) = \mathbf{V}_{\mathcal{F}}(\mathbf{c}^{(k+1)}) & k = 0, 1, \dots \end{cases} \tag{7}$$

with the following initial conditions (we shall henceforth consider these conditions to be understood)

$$\mathbf{d}^{(0)} = \mathbf{d}^{(-1)} = \mathbf{d}_0, \quad \mathbf{c}^{(0)} = \mathbf{c}_0. \tag{8}$$

Concerning the time advance of the two sub-models $\mathcal{S}$ and $\mathcal{F}$, we consider a fully implicit scheme for the former (due to its stiffness [19]), while for the latter we consider either an implicit scheme (setting $(\star) = (k+1)$) or an explicit one (setting $(\star) = (k)$).

ND scheme: Neumann (fluid) - Dirichlet (solid)

An alternative approach to the monolithic scheme is to solve the two models in a staggered way. A possible instance is:

$$\begin{cases} \mathcal{L}\left(\dfrac{\mathbf{d}^{(k+1)}-2\mathbf{d}^{(k)}+\mathbf{d}^{(k-1)}}{\Delta t^2}, \dfrac{\mathbf{d}^{(k+1)}-\mathbf{d}^{(k)}}{\Delta t}, \mathbf{d}^{(k+1)}, \mathbf{p}^{(k+1)}, t_{k+1}\right) = 0 \quad k=0,1,\dots \\ \mathbf{V}_{\mathcal{S}}(\mathbf{d}^{(k+1)}) = \mathbf{V}_{\mathcal{F}}(\mathbf{c}^{(k)}) \qquad\qquad k=0,1,\dots \\ \begin{cases} \dfrac{\mathbf{c}^{(k+1)}-\mathbf{c}^{(k)}}{\Delta t} = \mathbf{H}\left(\mathbf{c}^{(\star)}, \mathbf{p}^{(k+1)}, t_{k+1}\right) \quad k=0,1,\dots \end{cases} \end{cases} \tag{9}$$

At each time step we first update the variable $\mathbf{d}^{(k+1)}$, under the volume constraint $\mathbf{V}_{\mathcal{S}}(\mathbf{d}^{(k+1)}) = \mathbf{V}_{\mathcal{F}}(\mathbf{c}^{(k)})$. For this condition to be satisfied, the multiplier $\mathbf{p}^{(k+1)}$ must necessarily be determined simultaneously with $\mathbf{d}^{(k+1)}$. Successively, we update the variable $\mathbf{c}^{(k+1)}$ by employing the pressure vector $\mathbf{p}^{(k+1)}$ determined as above.

We denote the scheme as *Neumann-Dirichlet (ND)* scheme, as the fluid variable $\mathbf{c}$ is updated by assigning the pressure (which, in this context, can be regarded as a stress on the fluid), while the solid variable $\mathbf{d}$ is updated by assigning the volume (which amounts to prescribe the displacement).

DN scheme: Dirichlet (fluid) - Neumann (solid)

The dual of the ND scheme of Eq. (9) reads

$$\begin{cases} \dfrac{\mathbf{c}^{(k+1)}-\mathbf{c}^{(k)}}{\Delta t} = \mathbf{H}\left(\mathbf{c}^{(\star)}, \mathbf{p}^{(k+1)}, t_{k+1}\right) \quad k=0,1,\dots \\ \mathbf{V}_{\mathcal{F}}(\mathbf{c}^{(k+1)}) = \mathbf{V}_{\mathcal{S}}(\mathbf{d}^{(k)}) \qquad\qquad k=0,1,\dots \\ \begin{cases} \mathcal{L}\left(\dfrac{\mathbf{d}^{(k+1)}-2\mathbf{d}^{(k)}+\mathbf{d}^{(k-1)}}{\Delta t^2}, \dfrac{\mathbf{d}^{(k+1)}-\mathbf{d}^{(k)}}{\Delta t}, \mathbf{d}^{(k+1)}, \mathbf{p}^{(k+1)}, t_{k+1}\right) = 0 \quad k=0,1,\dots \end{cases} \end{cases} \tag{10}$$

Differently to the ND scheme, here the pressures $\mathbf{p}^{(k+1)}$ are determined simultaneously with the variable $\mathbf{c}^{(k+1)}$ of model $\mathcal{F}$, and are then passed to the model $\mathcal{S}$. For this reason, we call this scheme Dirichlet-Neumann (DN), since the fluid subproblem is solved with assigned volume (that is by controlling the displacement), while the structural subproblem is solved with assigned stress at the boundary.

3 Stability analysis

In this section, we study the numerical stability of the schemes presented in Sec. 2.2. With this goal, we introduce a minimal model, that is a simplified model of cardiac mechanics that features a minimal degree of complexity, but sufficient to reproduce a variety of behaviors exhibited by more comprehensive models.

3.1 A minimal model of cardiac mechanics

To define the minimal model $\mathcal{F}$–$\mathcal{S}$, we consider a zero-dimensional description of a single cardiac chamber, depicted in Fig. 1a. More precisely, we consider the following model of cardiac mechanics (model $\mathcal{S}$), where $V_{\mathcal{S}}(t)$ denotes the chamber volume and represents the unique state variable

$$\begin{cases} M\ddot{V}_{\mathcal{S}}(t) + C\dot{V}_{\mathcal{S}}(t) + p_{\text{pass}}(V_{\mathcal{S}}(t)) + A\,T_{\text{a}}(t) = p(t) \qquad t>0, \\ V_{\mathcal{S}}(0) = V_0,\ \dot{V}_{\mathcal{S}}(0) = 0. \end{cases} \tag{11}$$

This model accounts for both inertia and viscous damping, through the coefficients $M \geq 0$ and $C \geq 0$, respectively. The coefficient $A \geq 0$ is associated with the active force generated by the muscle. Finally $p_{\text{pass}}(V_{\mathcal{S}})$ represents the steady-state pressure corresponding to a given volume $V_{\mathcal{S}}$ when the chamber is

fully relaxed (i.e. $T_a = 0$). It thus corresponds to the end-diastolic (ED) pressure-volume relationship, also known as Klotz's curve [26]. The function p_{pass} should be constitutively prescribed and it represents the 0D fingerprint of the 3D hyperelastic constitutive law.

Concerning the model $\mathcal{F}$, we connect the cardiac chamber to a valve and we consider a prescribed external pressure $p_{ext}(t)$. Thus, the chamber volume $V_{\mathcal{F}}(t)$ evolves according to following simple fluid model (model $\mathcal{F}$):

$$\begin{cases} \dot{V}_{\mathcal{F}}(t) = Q_{valve}(p_{ext}(t) - p(t)) & t > 0, \\ V_{\mathcal{F}}(0) = V_0, \end{cases} \tag{12}$$

where Q_{valve} is given by either Q^{out}_{valve} or Q^{in}_{valve}:

$$Q^{out}_{valve}(\Delta p) = \begin{cases} \dfrac{\Delta p}{R_{min}}, & \text{if } \Delta p < 0, \\ \dfrac{\Delta p}{R_{max}}, & \text{if } \Delta p \geq 0, \end{cases}, \qquad Q^{in}_{valve}(\Delta p) = \begin{cases} \dfrac{\Delta p}{R_{max}}, & \text{if } \Delta p < 0, \\ \dfrac{\Delta p}{R_{min}}, & \text{if } \Delta p \geq 0, \end{cases} \tag{13}$$

where $R_{max} \gg 1$ and $R_{min} \ll 1$ represent the hemodynamic resistances corresponding to a closed and open valve, respectively. The function Q^{out}_{valve} (respectively, Q^{in}_{valve}) describe an outflow (respectively, inflow) valve. Indeed, the valve is open in case of negative (respectively, positive) pressure gradient and vice versa.

Hence, the coupled minimal model $\mathcal{F}$–$\mathcal{S}$ reads

$$\begin{cases} M\ddot{V}_{\mathcal{S}}(t) + C\dot{V}_{\mathcal{S}}(t) + p_{pass}(V_{\mathcal{S}}(t)) + A\,T_a(t) = p(t) & t > 0, \\ \dot{V}_{\mathcal{F}}(t) = Q_{valve}(p_{ext}(t) - p(t)) & t > 0, \\ V_{\mathcal{S}}(t) = V_{\mathcal{F}}(t) & t > 0, \\ V_{\mathcal{S}}(0) = V_0,\ \dot{V}_{\mathcal{S}}(0) = 0,\ V_{\mathcal{F}}(0) = V_0, \end{cases} \tag{14}$$

which represents a particular case of Eq. (6), provided we adopt the following identification for the (one-dimensional) state variables $\mathbf{d}(t) = [V_{\mathcal{S}}(t)]$ and $\mathbf{c}(t) = [V_{\mathcal{F}}(t)]$. A further abstraction of the cardiac mechanics minimal model (14) is the piston problem in Fig. 1b. This is formally obtained from the model (14), by employing the linearly elastic law $p_{pass}(V_{\mathcal{S}}) = E(V_{\mathcal{S}} - V_0)$, where $E > 0$ is known as elastance and V_0 is the resting volume, by neglecting active force and by assuming a constant fluid flow resistance R.

The ND scheme applied to the minimal model (14) reads

$$\begin{cases} M\dfrac{V_{\mathcal{S}}^{(k+1)} - 2V_{\mathcal{S}}^{(k)} + V_{\mathcal{S}}^{(k-1)}}{\Delta t^2} + C\dfrac{V_{\mathcal{S}}^{(k+1)} - V_{\mathcal{S}}^{(k)}}{\Delta t} + p_{pass}(V_{\mathcal{S}}^{(k+1)}) + A\,T_a(t_{k+1}) = p^{(k+1)} & k = 0, 1, \dots \\ V_{\mathcal{S}}^{(k+1)} = V_{\mathcal{F}}^{(k)} & k = 0, 1, \dots \\ \dfrac{V_{\mathcal{F}}^{(k+1)} - V_{\mathcal{F}}^{(k)}}{\Delta t} = Q_{valve}(p_{ext}(t_{k+1}) - p^{(k+1)}) & k = 0, 1, \dots \end{cases} \tag{15}$$

with initial conditions

$$V_{\mathcal{S}}^{(0)} = V_{\mathcal{S}}^{(-1)} = V_{\mathcal{F}}^{(0)} = V_0.$$

Conversely, the DN scheme reads (with the same initial conditions as above)

$$\begin{cases} \dfrac{V_{\mathcal{F}}^{(k+1)} - V_{\mathcal{F}}^{(k)}}{\Delta t} = Q_{valve}(p_{ext}(t_{k+1}) - p^{(k+1)}) & k = 0, 1, \dots \\ V_{\mathcal{F}}^{(k+1)} = V_{\mathcal{S}}^{(k)} & k = 0, 1, \dots \\ M\dfrac{V_{\mathcal{S}}^{(k+1)} - 2V_{\mathcal{S}}^{(k)} + V_{\mathcal{S}}^{(k-1)}}{\Delta t^2} + C\dfrac{V_{\mathcal{S}}^{(k+1)} - V_{\mathcal{S}}^{(k)}}{\Delta t} + p_{pass}(V_{\mathcal{S}}^{(k+1)}) + A\,T_a(t_{k+1}) = p^{(k+1)} & k = 0, 1, \dots \end{cases} \tag{16}$$

3.2 Definitions and lemmas

Before studying the numerical stability of the schemes (15) and (16), we recall the definition of zero-stability and absolute stability of a numerical scheme [36]. The definitions refer to the following abstract problem, where $\boldsymbol{\psi}^{(k)} \in \mathbb{R}^d$ denotes the state variable at time t_k:

$$\begin{cases} \boldsymbol{\psi}^{(k)} = \Phi(\boldsymbol{\psi}^{(k-1)}, t_k, \Delta t) & k = 1, 2, \dots \\ \boldsymbol{\psi}^{(0)} = \boldsymbol{\psi}_0, \end{cases} \tag{17}$$

We notice that both the ND an DN schemes are particular cases of Eq. (17), as we show in Sec. 3.3. We then consider the perturbed problem:

$$\begin{cases} \widetilde{\boldsymbol{\psi}}^{(k)} = \Phi(\widetilde{\boldsymbol{\psi}}^{(k-1)}, t_k, \Delta t) + \Delta t\, \boldsymbol{\eta}^{(k)} & k = 1, 2, \dots \\ \widetilde{\boldsymbol{\psi}}^{(0)} = \boldsymbol{\psi}_0 + \boldsymbol{\eta}^{(0)}, \end{cases} \tag{18}$$

where $\boldsymbol{\eta}^{(k)}$ denotes a suitable perturbation. We consider the following definitions [36].

Definition 1 (zero-stability)**.** *Let us consider a finite time $T > 0$ and a uniform subdivision of the time interval $(0, T)$ into N subintervals, i.e. $\Delta t = T/N$. The numerical scheme* (17) *is said zero-stable if*

$$\exists\, \Delta t_0 > 0,\, \exists\, C > 0 : \qquad \sup_{k=0,\dots,N} |\widetilde{\boldsymbol{\psi}}^{(k)} - \boldsymbol{\psi}^{(k)}| \leq C(T) \sup_{k=0,\dots,N} |\boldsymbol{\eta}^{(k)}| \qquad \forall\, \Delta t \in (0, \Delta t_0],$$

where $\boldsymbol{\psi}^{(k)}$ and $\widetilde{\boldsymbol{\psi}}^{(k)}$ are solutions to problems (17) *and* (18)*, respectively.*

Definition 2 (absolute stability)**.** *Let us consider a given time step size $\Delta t > 0$. We consider the solution of the numerical problem for $t_k \to +\infty$. The numerical scheme* (17) *is said absolutely stable in correspondence to Δt if*

$$\exists\, C > 0 : \qquad \lim_{k \to +\infty} |\widetilde{\boldsymbol{\psi}}^{(k)} - \boldsymbol{\psi}^{(k)}| \leq C \sup_{k \geq 0} |\boldsymbol{\eta}^{(k)}|,$$

where $\boldsymbol{\psi}^{(k)}$ and $\widetilde{\boldsymbol{\psi}}^{(k)}$ are solutions to problems (17) *and* (18)*, respectively. Moreover, we say that the method is unconditionally absolutely stable if it is absolutely stable for any $\Delta t > 0$.*

The zero-stability property of a scheme guarantees that its solution does not blow up on a finite time horizon when $\Delta t \to 0^+$. This is particular entails that the noise introduced by round-off errors is not amplified. The absolute stability property deals instead with the behavior of the solution for $t \to +\infty$. Unconditional absolute stability is a stronger notion than zero-stability [36].

The stability properties of a numerical scheme in the form (17) can be linked with the spectral properties of the Jacobian matrix of the iteration function Φ. Specifically, they are linked with its spectral radius (i.e. the modulus of the largest eigenvalue), denoted by $\rho(\cdot)$. We recall the following result, proved in [45]:

Lemma 1 (Prop. 1 of [45])**.** *Let us consider the numerical scheme* (17) *with $\Phi \colon \mathbb{R}^d \times \mathbb{R}^+ \times \mathbb{R}^+ \to \mathbb{R}^d$ differentiable with respect to its first argument. If the condition*

$$\exists\, \Delta t_0 > 0,\, \exists\, \alpha \in \mathbb{R} \colon \quad \rho\left(\frac{\partial \Phi(\boldsymbol{\psi}, t, \Delta t)}{\partial \boldsymbol{\psi}}\right) \leq 1 + \alpha\, \Delta t \quad \forall\, \boldsymbol{\psi} \in \mathbb{R}^d,\, t \geq 0,\, \Delta t \in (0, \Delta t_0] \tag{19}$$

holds true, then the scheme (17) *is zero-stable. Moreover, if for a given Δt the condition*

$$\exists\, \rho_0 < 1 \colon \qquad \rho\left(\frac{\partial \Phi(\boldsymbol{\psi}, t, \Delta t)}{\partial \boldsymbol{\psi}}\right) \leq \rho_0 \qquad \forall\, \boldsymbol{\psi} \in \mathbb{R}^d,\, t \geq 0, \tag{20}$$

holds true, then the scheme is absolutely stable in correspondence to Δt.

We have then the following result.

Lemma 2. *Let us suppose that the iteration function Φ in Eq. (17) is assigned implicitly by*

$$\mathcal{H}(\boldsymbol{\psi}^{(k)}, \boldsymbol{\psi}^{(k-1)}, t_k, \Delta t) = \mathbf{0} \qquad k = 1, 2, \dots \tag{21}$$

where $\mathcal{H}\colon \mathbb{R}^d \times \mathbb{R}^d \times \mathbb{R}^+ \times \mathbb{R}^+ \to \mathbb{R}^d$ is continuously differentiable in its first argument and differentiable with respect to the second one. We define, for $\boldsymbol{\psi}_2, \boldsymbol{\psi}_1 \in \mathbb{R}^d$, $t > 0$, $\Delta t > 0$:

$$\begin{aligned} \mathbf{A}(\boldsymbol{\psi}_2, \boldsymbol{\psi}_1, t, \Delta t) &:= \frac{\partial \mathcal{H}(\boldsymbol{\psi}_2, \boldsymbol{\psi}_1, t, \Delta t)}{\partial \boldsymbol{\psi}_2} \in \mathbb{R}^{d\times d}, \\ \mathbf{B}(\boldsymbol{\psi}_2, \boldsymbol{\psi}_1, t, \Delta t) &:= \frac{\partial \mathcal{H}(\boldsymbol{\psi}_2, \boldsymbol{\psi}_1, t, \Delta t)}{\partial \boldsymbol{\psi}_1} \in \mathbb{R}^{d\times d}. \end{aligned} \tag{22}$$

Then, if $\mathbf{A}(\boldsymbol{\psi}_2, \boldsymbol{\psi}_1, t, \Delta t)$ is non-singular, the Jacobian matrix of the iteration function is given by

$$\frac{\partial \Phi(\boldsymbol{\psi}_1, t, \Delta t)}{\partial \boldsymbol{\psi}_1} = -\mathbf{A}^{-1}(\boldsymbol{\psi}_2, \boldsymbol{\psi}_1, t, \Delta t)\mathbf{B}(\boldsymbol{\psi}_2, \boldsymbol{\psi}_1, t, \Delta t)$$

where $\boldsymbol{\psi}_2 = \Phi(\boldsymbol{\psi}_1, t, \Delta t)$.

Proof. This is a direct consequence of the implicit function theorem (see e.g. [27]). □

Thanks to Lemmas 1 and 2, both zero-stability and absolute stability of a numerical scheme assigned in implicit form (such as the ND and DN schemes of Eqs. (9) and (10)) can be linked with the spectral properties of the Jacobian matrix $-\mathbf{A}^{-1}\mathbf{B}$. In particular, a spectral radius strictly lower than 1 entails absolute stability (and hence zero-stability).

3.3 Spectral analysis

We now study, on the basis of the results of Sec. 3.2, the numerical stability of the ND and DN of Eqs. (15) and (16). We observe that both the schemes can be recast in the abstract form (17), provided that we define, for $k \geq 0$, the state vector $\boldsymbol{\psi}^{(k)} := (V_{\mathcal{S}}^{(k)}, V_{\mathcal{S}}^{(k-1)}, V_{\mathcal{F}}^{(k)}, p^{(k)})^T$. The matrices $\mathbf{A}$ and $\mathbf{B}$, for the ND and DN schemes, are respectively given by

$$\begin{aligned} \mathbf{A}_{\mathrm{ND}} &= \begin{pmatrix} E + \frac{M}{\Delta t^2} + \frac{C}{\Delta t} & -\frac{M}{\Delta t^2} & 0 & -1 \\ 0 & 1 & 0 & 0 \\ 0 & 0 & \Delta t^{-1} & R^{-1} \\ 1 & 0 & 0 & 0 \end{pmatrix}; \quad \mathbf{B}_{\mathrm{ND}} = \begin{pmatrix} -\left(\frac{M}{\Delta t^2} + \frac{C}{\Delta t}\right) & \frac{M}{\Delta t^2} & 0 & 0 \\ -1 & 0 & 0 & 0 \\ 0 & 0 & -\Delta t^{-1} & 0 \\ 0 & 0 & -1 & 0 \end{pmatrix}; \\ \mathbf{A}_{\mathrm{DN}} &= \begin{pmatrix} E + \frac{M}{\Delta t^2} + \frac{C}{\Delta t} & -\frac{M}{\Delta t^2} & 0 & -1 \\ 0 & 1 & 0 & 0 \\ 0 & 0 & \Delta t^{-1} & R^{-1} \\ 0 & 0 & -1 & 0 \end{pmatrix}; \quad \mathbf{B}_{\mathrm{DN}} = \begin{pmatrix} -\left(\frac{M}{\Delta t^2} + \frac{C}{\Delta t}\right) & \frac{M}{\Delta t^2} & 0 & 0 \\ -1 & 0 & 0 & 0 \\ 0 & 0 & -\Delta t^{-1} & 0 \\ 1 & 0 & 0 & 0 \end{pmatrix}. \end{aligned} \tag{23}$$

We have defined

$$E(V_{\mathcal{S}}) = E_{\mathrm{pass}}(V_{\mathcal{S}}) = p'_{\mathrm{pass}}(V_{\mathcal{S}})$$

as the elastance of the cardiac chamber, while R denotes either $R_{\min}$ or $R_{\max}$, depending on whether the valve is open or closed. As E and R depend on the current state, also $\mathbf{A}$ depends on the state. Nonetheless, we will leave this dependence as understood.

We now numerically study the spectrum of the Jacobian matrix $-\mathbf{A}^{-1}\mathbf{B}$, for different parameters values. As reference values, we consider those given in Tab. 1, which correspond to realistic values for the mechanics of a human left ventricle (see Appendix A). In particular, we investigate the effect of inertia ($M \neq 0$) and viscous damping ($C \neq 0$), compared to a quasi-static formulation of the structure mechanics problem ($M = C = 0$). First, in Sec. 3.3.1, we consider the case of closed valve ($R = R_{\max}$); then, in Sec. 3.3.2, that of open valve ($R = R_{\min}$).

Parameter	Measure unit	Value
$\overline{E}_{\text{pass}}$	$\text{mmHg}\,\text{mL}^{-1}$	0.09
$\overline{E}_{\text{act}}$	$\text{mmHg}\,\text{mL}^{-1}$	36
$\overline{C}$	$\text{mmHg}\,\text{mL}^{-1}\,\text{ms}$	24
$\overline{M}$	$\text{mmHg}\,\text{mL}^{-1}\,\text{ms}^2$	8.6
R_{max}	$\text{mmHg}\,\text{mL}^{-1}\,\text{s}$	$7.5 \cdot 10^4$
R_{min}	$\text{mmHg}\,\text{mL}^{-1}\,\text{s}$	$7.5 \cdot 10^{-3}$

Table 1: Reference parameters of the minimal model of Eq. (11). These values are derived in Appendices A and B by means of a 0D reduction of the 3D cardiac mechanics model described in Sec. 5.2.1.

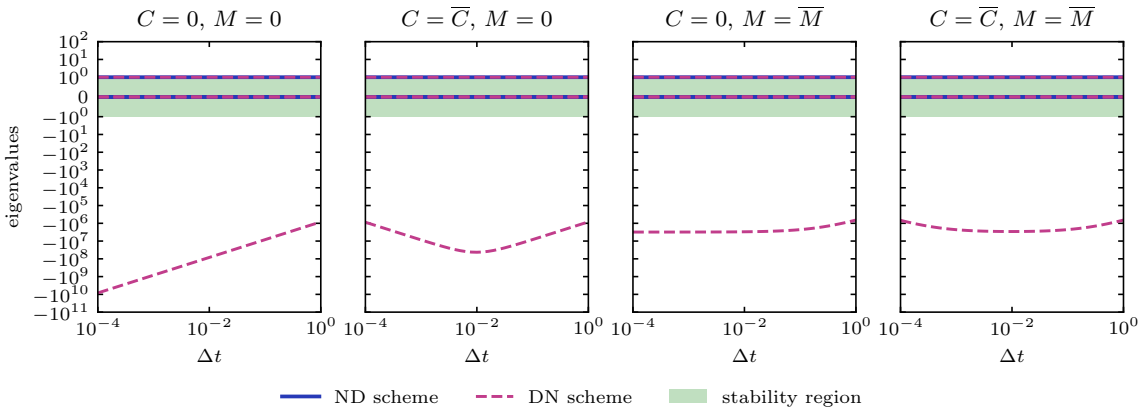

Figure 4: Eigenvalues of the Jacobian matrix $-\mathbf{A}^{-1}\mathbf{B}$ for the ND and DN schemes in the closed valve case ($R = R_{\text{max}}$, $E = \overline{E}_{\text{pass}}$). From left to right: quasi-static case, only viscosity enabled, only inertia enable, both viscosity and inertia enabled.

3.3.1 Closed valve

Let us consider the case of a closed valve (which corresponds to $R = R_{\text{max}}$). In Fig. 4 we show the dependence of the eigenvalues of $-\mathbf{A}^{-1}\mathbf{B}$ on the time step size Δt, in the quasi-static case and when adding inertia and/or viscosity. We observe that in all the cases, the ND scheme has all eigenvalues with modulus less than one and it is therefore numerically stable. The DN scheme, instead, has a very large negative eigenvalue ($\mu < -10^5$). Adding inertia and viscosity slightly lowers its magnitude, which however is still very high).

The instability of the DN scheme when the valve is closed is due to the balloon dilemma [5, 20], that is the impossibility of satisfying the incompressibility constraint when the pressure is assigned. As a matter of fact, by considering for simplicity the quasi-static case ($C = M = 0$), the eigenvalues of the Jacobian matrix $-\mathbf{A}^{-1}\mathbf{B}$ read

$$\mu_{\pm} = \frac{R_{\text{max}}}{2E\Delta t}\left(\pm\sqrt{1 + \frac{4E\Delta t}{R_{\text{max}}}} - 1\right).$$

When we approach the incompressible limit (i.e. for $R_{\text{max}} \to +\infty$), $\mu_+ \to 1^-$ and $\mu_- \to -\infty$. Hence, the more the valve resists blood flow, the greater the magnitude of the numerical oscillations will be, because of the eigenvalue $\mu_- \to -\infty$. This provides in fact an algebraic interpretation of the balloon dilemma.

3.3.2 Open valve

Let us now consider the case of an open valve (corresponding to $R = R_{\text{min}}$). In the case of quasi-static mechanics, as shown in the left-most plot of Fig. 5, the ND scheme is absolutely stable for small Δt, and unstable for large Δt, while the DN scheme has opposite behavior. More precisely, there exists a critical

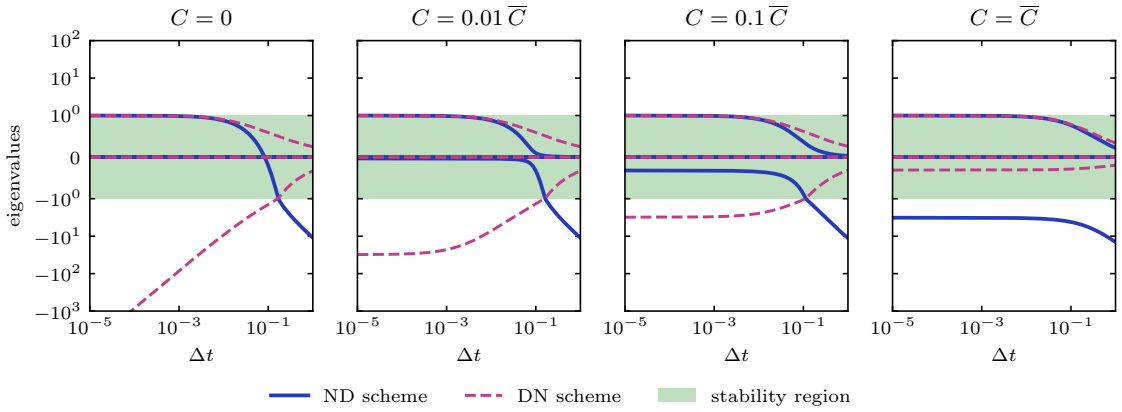

Figure 5: Eigenvalues of the Jacobian matrix $-\mathbf{A}^{-1}\mathbf{B}$ for the ND and DN schemes in the open valve case and without inertia ($R = R_{\min}$, $E = \overline{E}_{\text{pass}}$, $M = 0$), for increasing viscosity (see titles).

Δt that acts as threshold of absolute stability for the two schemes ND and DN (for the parameter values here considered, it is approximately $\Delta t = 0.1\,\text{s}$). Moreover, as the zero-stability property of a scheme deals with its behavior for $\Delta t \to 0^+$ (see Def. 1), the ND scheme, unlike the DN scheme, is zero-stable.

We now study the effect of inertia and viscosity. In Fig. 5 we consider the spectrum in the case $M = 0$ and for increasing viscosity. Similarly, in Fig. 6, we set $C = 0$ and we consider increasing values of M (increasing inertia). The presence of either viscosity or inertia is able to stabilize the DN scheme, whereas it worsens the stability properties of the ND scheme. More precisely, both viscosity and inertia introduce in the spectrum associated with the ND scheme an eigenvalue with negative real part, which, for some values of Δt, has modulus greater than 1 thus making the ND scheme unstable. Moreover, Fig. 5 shows that there is a critical viscosity value, above which the ND scheme is never stable. Instead, inertia makes the ND scheme unstable for low values of Δt (see Fig. 6). Therefore, when inertia is present, the scheme turns out to be absolutely stable only in an interval of values of Δt, which gets narrower and narrower as M increases. We notice that, since for $\Delta t \to 0^+$ inertia always yields an eigenvalue of modulus greater than 1, the presence of inertia makes the ND scheme to be non zero-stable.

Finally, in Fig. 7 we show the combined effects of viscosity and inertia. This is in line with the results obtained above: the presence of viscosity and inertia improves the stability of the DN scheme and worsens that of the ND scheme.

3.3.3 The effect of active stress

In the minimal model (11), the amount of active stress $T_a(t)$ is prescribed. However, very often in the literature, the active stress is computed by means of suitable models describing the subcellular activity of cardiomyocytes [30, 41, 47]. These models are typically characterized by a feedback from the myocardial mechanics model: when the tissue rapidly contracts, the force generated decreases [40]. For this reason, we now investigate the effect that this feedback may have on the stability analysis conducted above.

At the macroscopic level, the effect of the feedback acting from tissue mechanics to force generation is known as force-velocity relationship and was first observed by the Nobel laureate Archibald V. Hill in 1938 [22]. Its origin lies in fact at the microscopic level. The active force is generated by a very large number (approximately 10^8 per mm^3 of tissue) of crossbridges, that is bounded actin-myosin pairs. Each myosin protein, due to its elasticity, acts as a microscopic spring, thus producing the active force observable at the macroscopic level. The presence of these actin-myosin bonds not only generates a net force in the direction of the cardiac fibres, but also has the effect of opposing rapid changes in fibre length (whence the force-velocity relationship observed by A. V. Hill). Their action therefore results in an increased stiffness of the tissue.

As a matter of fact, the active stiffness (that is the amount of stiffness associated with attached crossbridges) can be computed from the active force generation at hand. Let us consider a generic force

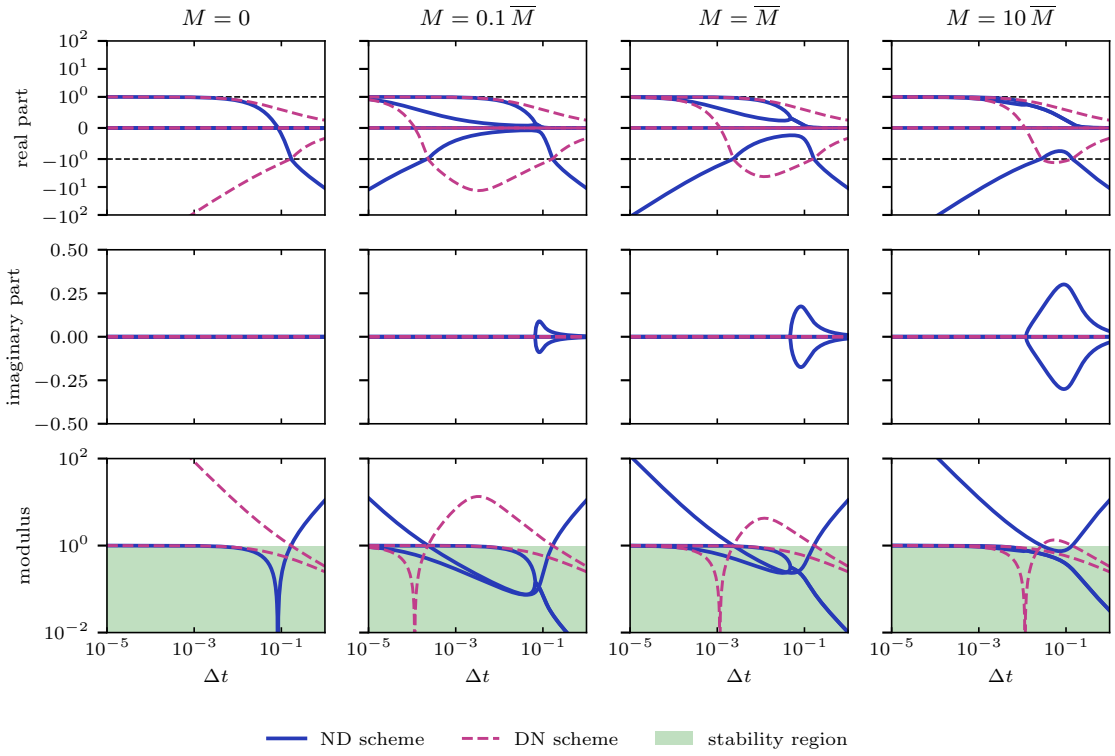

Figure 6: Eigenvalues of the Jacobian matrix $-\mathbf{A}^{-1}\mathbf{B}$ for the ND and DN schemes in the open valve case and without viscosity ($R = R_{\min}$, $E = \overline{E}_{\text{pass}}$, $C = 0$), for increasing inertia (see titles).

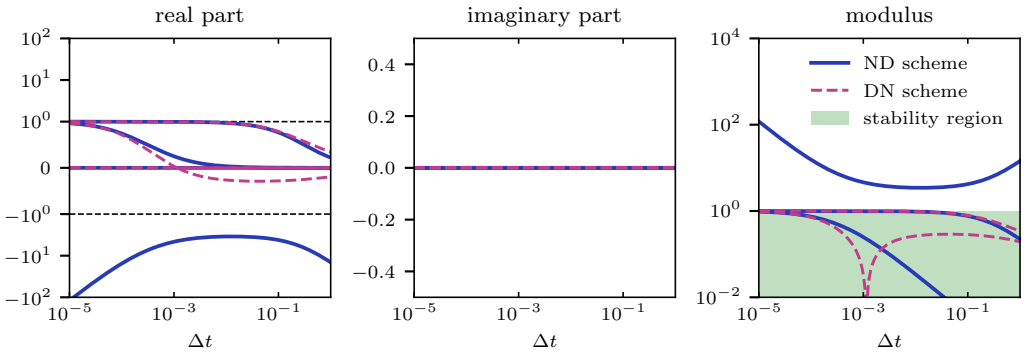

Figure 7: Eigenvalues of the Jacobian matrix $-\mathbf{A}^{-1}\mathbf{B}$ for the ND and DN schemes in the open valve case, in presence of both viscosity and inertia ($R = R_{\min}$, $E = \overline{E}_{\text{pass}}$, $C = \overline{C}$, $M = \overline{M}$).

generation model, in the following form (that encompasses most of the models available in literature, see e.g. [29, 30, 33, 41, 46])

$$\begin{cases} \dot{\mathbf{r}}(t) = \mathbf{h}\left(\mathbf{r}(t), c(t), \lambda(t), \dot{\lambda}(t)\right), & t > 0, \\ T_{\mathrm{a}}(t) = g\left(\mathbf{r}(t)\right), & t > 0, \\ \mathbf{r}(0) = \mathbf{r}_0, \end{cases} \tag{24}$$

where $\mathbf{r}(t)$ is the state variables vector, $c(t)$ is the intracellular calcium concentration (an input of the model, often denoted by $[\mathrm{Ca}^{2+}]_{\mathrm{i}}$), while $\lambda = \sqrt{I_{4f}} - 1$ represents the tissue strain in the fiber direction. Finally, $\mathbf{h}$ and g are suitable functions. As shown in [45], the active stiffness (henceforth denoted as K_{a}) is given by

$$K_{\mathrm{a}} = \frac{\partial \dot{T}_{\mathrm{a}}}{\partial \dot{\lambda}} = \nabla_{\mathbf{r}} g \cdot \frac{\partial \mathbf{h}}{\partial \dot{\lambda}}. \tag{25}$$

To study the effect of using a force generation model as in Eq. (24) on the stability of the numerical schemes considered in this paper, we proceed as follows. First, we consider the coupled model obtained by pairing the minimal model of Eq. (14) with Eq. (24). Then, we study the spectrum of the Jacobian matrix $-\mathbf{A}^{-1}\mathbf{B}$ associated with the numerical discretization of this coupled model and we apply Lemma 1. In Appendix B we report the detailed calculations in this regard and we here report only the final result. We show that adding an active mechanics model has the equivalent effect of increasing the passive elastance E_{pass}. More precisely, we obtain matrices equivalent to Eq. (23), but where the passive elastance E_{pass} is replaced by an augmented elastance given by $E = E_{\mathrm{pass}} + E_{\mathrm{act}}$. As a matter of fact, the active elastance E_{act} is proportional to the active stiffness K_{a}. This result is not surprising, but on the contrary it is in line with the microscopic interpretation of the force-velocity relationship mentioned above, whereby the latter results from an increase in microscopic stiffness due to attached crossbridges.

The above remarks also makes it possible to apply the results of Sec. 3.3 to the case of using force generation models that take into account the force-velocity relationship, provided that we consider a suitably augmented elastance. In fact, at the peak of systole, active elastance E_{act} is much larger than passive elastance E_{pass} (up to 400 times greater, see Appendix B). This implies that using a force generation model with force-velocity relationship, rather than using a prescribed force transient, might substantially impact the numerical stability of the scheme in use.

In Fig. 8 we study the eigenvalues of the Jacobian matrix $-\mathbf{A}^{-1}\mathbf{B}$ for both the ND and DN schemes for increasing values of the total elastance E. Specifically, we move from the case when the tissue is fully deactivated ($E = \overline{E}_{\mathrm{pass}}$) to the case of full activation ($E = \overline{E}_{\mathrm{pass}} + \overline{E}_{\mathrm{act}}$). Intermediate values correspond to a partial activation of the tissue. The results show that the presence of an active stress betters the stability properties of the DN scheme, while it worsen those of the ND scheme. Let us consider for instance the quasi-static case (forst row of Fig. 8). When the tissue if not activated, the ND scheme is absolutely stable if and only if $\Delta t < \overline{\Delta t}$, where the stability threshold is approximately $\overline{\Delta t} \simeq 2 \cdot 10^{-1}$ s. When the tissue is fully activated, however, the stability threshold is much stricter ($\overline{\Delta t} \simeq 5 \cdot 10^{-4}$ s).

3.4 Analysis of the non-physical oscillations

The spectral analysis of Sec. 3.3 allowed us to identify the ranges of parameters and of Δt for which the ND and DN schemes are either stable or unstable. We now analyze, in light of the results of Sec. 3.3, the non-physical oscillations that can occur using the two ND and DN schemes, when the stability conditions are not met. The occurrence of these oscillations is represented schematically in Fig. 9.

Let us first consider the ND scheme (first row of Fig. 9). At the first step (ND-a), since the external pressure (p_{ext}) is higher than the chamber pressure (p), the fluid model predicts a blood flow Q towards the chamber and a consequent increase in volume V. At the next step (ND-b), the structure mechanics model receives as an input the volume calculated at step ND-a and generates, due to the increase in volume, an increase in pressure. If the time step length Δt is sufficiently large, the pressure increase is such that p is now greater than p_{ext}, thus generating a backflow at the fluid substep ND-c, which leads to a decrease in volume. At step ND-d the pressure must necessarily drop, thus returning to the state represented in step ND-a and the cycle is repeated. The onset of oscillations is therefore related to the amplitude of pressure jumps occurring in ND-b and ND-d. If these are large enough to reverse

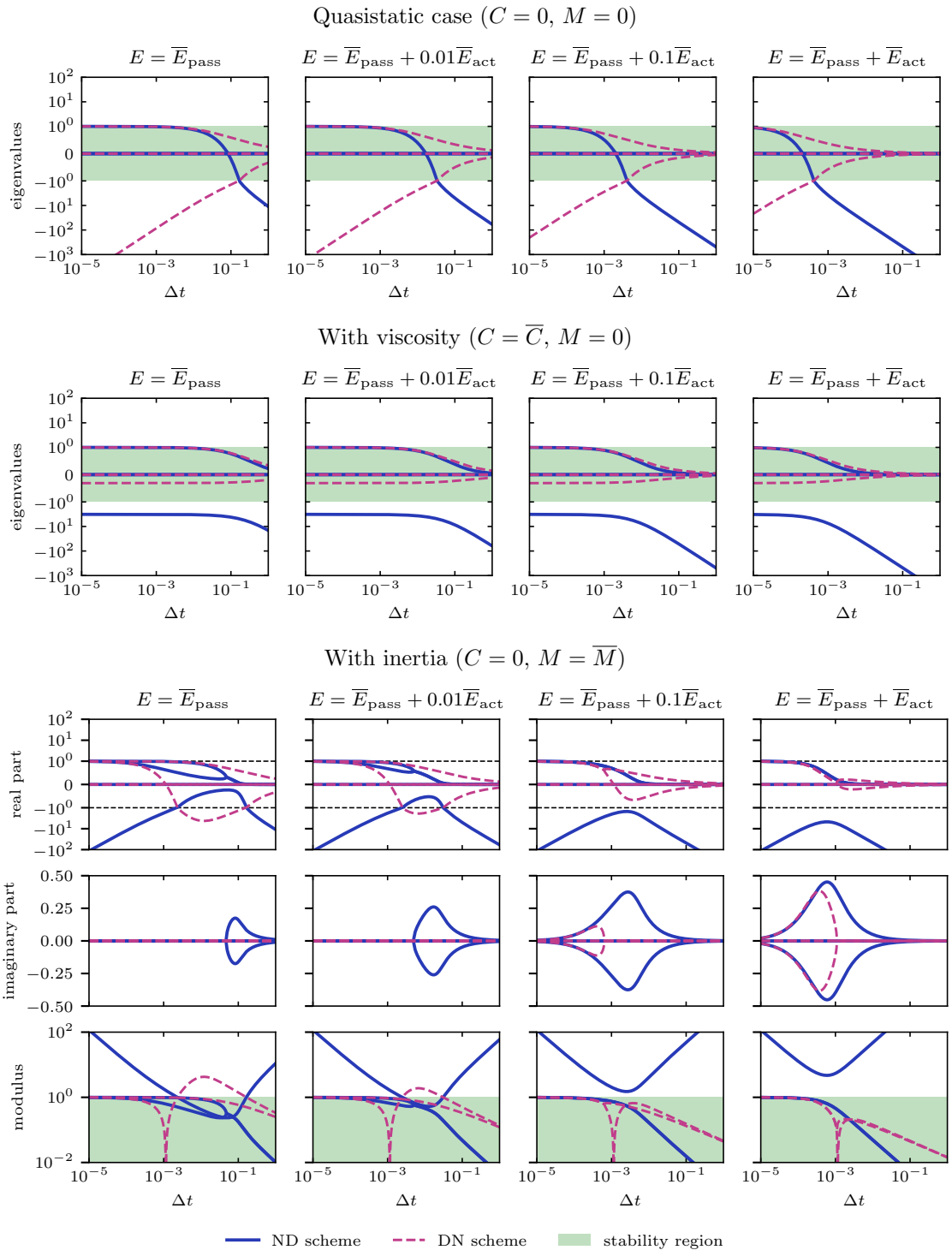

Figure 8: Eigenvalues of the Jacobian matrix $-\mathbf{A}^{-1}\mathbf{B}$ for the ND and DN schemes in the open valve case ($R = R_{\text{min}}$), for incresing elastance (see titles).

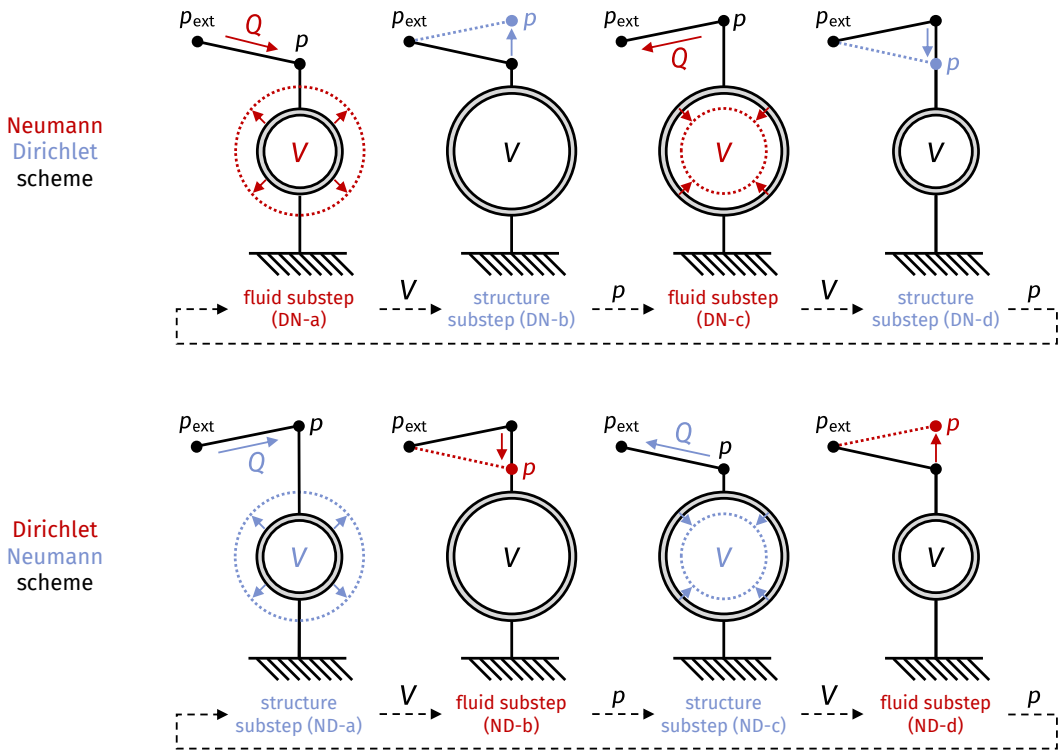

Figure 9: Schematic representation of the oscillations occurring with the ND scheme (top) and with the DN scheme (bottom). The substeps associated with the solution of the structure mechanics problem (model $\mathcal{S}$) are shown in blue, while those related to the fluid problem (model $\mathcal{F}$) are shown in red. The chamber is represented as a balloon, with a volume V associated with it. The height of the bullet above the balloon symbolizes the associated pressure, while the bullet on the left represents the external pressure. When the latter is higher, there is a positive pressure gradient between the outer and inner regions of the chamber; when it is lower, the pressure gradient is negative.

the sign of the pressure gradient, nonphysical oscillations occur. It is clear that a large pressure jump is favored by a small value of Δt and by a large value of the elastance E. This is in line with the results in Sec. 3.3. Moreover, when viscosity or inertia are included into the model, the cardiac chamber opposes rapid changes in volume more strongly. Therefore, in ND-b and ND-d, where a volume change is imposed, the larger the inertia or viscosity, the larger the pressure jump with which the model responds. This is also in line with the findings of Sec. 3.3, predicting that, when using the ND scheme, the presence of viscosity or inertia makes it more likely that oscillations will occur.

Conversely, in the DN scheme (second row of Fig. 9), the pressure is determined by the fluid model, which receives volume changes as input from the structure mechanics model. In this case, therefore, large elastance (E), viscosity (C) or stiffness (M) hamper the non-physical oscillations. In fact, each of these factors causes the structure mechanics model to respond with smaller volume changes to a given pressure change, thus preventing numerical instabilities from being generated. This is also consistent with the results of the spectral analysis of Sec. 3.3, whereby the DN scheme enjoys better stability properties when either E, C or M are large.

4 Stabilized scheme

In this section, we propose a numerical scheme that cures the numerical instabilities analyzed in Sec. 3. First, in Sec. 4.1, we present the rationale behind its derivation. Then, we study its stability properties using the tools introduced in Sec. 3.2, by considering the minimal model (Sec. 4.2). Finally, in Sec. 4.3, we generalize the result for a generic structure model.

4.1 Derivation of the stabilized scheme (ND-stab)

The analysis of Sec. 3 revealed that the DN scheme might feature eigenvalues with a very large modulus (this is related to the balloon dilemma, see Sec. 3.3.1). In comparison, the worst case of the ND scheme has less severe instabilities issues. For this reason, we focus on the latter scheme, and we aim to find a stabilization term that cures the numerical oscillations that might occur.

Following the analysis of Sec. 3.4, the non-physical oscillations are related to the structure mechanics substep, which updates the pressure while being unaware of the effect the pressure update will have on the volume change within the next fluid substep. A too large change in pressure might indeed reverse the flux through the valve. To cure this issue, we porpose to incorporate, within the structure mechanics substep, a prediction of the volume variation due to the net blood flux that will be generated within the next fluid substep. Specifically, within (15), we replace the equation

$$V_{\mathcal{S}}^{(k+1)} = V_{\mathcal{F}}^{(k)} \tag{26}$$

by the equation

$$V_{\mathcal{S}}^{(k+1)} = V_{\mathcal{F}}^{(k)} + \Delta t\, Q_{\text{stab}}(p^{(k+1)}, t_{k+1}). \tag{27}$$

having defined

$$Q_{\text{stab}}(p,t) = Q_{\text{valve}}(p_{\text{ext}}(t) - p).$$

The additional term $\Delta t\, Q_{\text{stab}}$ plays the role of a stabilization term. We remark that this term is clearly numerically consistent, as it tends to zero when $\Delta t \to 0^+$ (see e.g. [39]). The stabilized ND scheme (henceforth denoted by ND-stab scheme), then reads

$$\begin{cases} M\dfrac{V_{\mathcal{S}}^{(k+1)} - 2V_{\mathcal{S}}^{(k)} + V_{\mathcal{S}}^{(k-1)}}{\Delta t^2} + C\dfrac{V_{\mathcal{S}}^{(k+1)} - V_{\mathcal{S}}^{(k)}}{\Delta t} + p_{\text{pass}}(V_{\mathcal{S}}^{(k+1)}) + A\,T_{\text{a}}(t_{k+1}) = p^{(k+1)} & k = 0, 1, \dots \\ V_{\mathcal{S}}^{(k+1)} = V_{\mathcal{F}}^{(k)} + \Delta t\, Q_{\text{stab}}(p^{(k+1)}, t_{k+1}) & k = 0, 1, \dots \\ \dfrac{V_{\mathcal{F}}^{(k+1)} - V_{\mathcal{F}}^{(k)}}{\Delta t} = Q_{\text{valve}}(p_{\text{ext}}(t_{k+1}) - p^{(k+1)}) & k = 0, 1, \dots \end{cases} \tag{28}$$

We remark that the ND-stab scheme preserves the staggered structure of the ND scheme, as the newly introduced term does not involve the fluid state variable $V_{\mathcal{F}}^{(k+1)}$.

4.2 Stability analysis of the ND-stab scheme

We now study the numerical stability of the ND-stab scheme of Eq. (28), based on the lemmas of Sec. 3.2. With reference to Lemma 2, the $\mathbf{B}$ matrix of the ND-stab scheme coincides with that of the ND scheme (see Eq. (23)), while the $\mathbf{A}$ matrix changes as follows

$$\mathbf{A}_{\text{ND}-\text{stab}} = \mathbf{A}_{\text{ND}} + \begin{pmatrix} 0 & 0 & 0 & 0 \\ 0 & 0 & 0 & 0 \\ 0 & 0 & 0 & 0 \\ 0 & 0 & 0 & \frac{\Delta t}{R} \end{pmatrix}, \qquad \mathbf{B}_{\text{ND}-\text{stab}} = \mathbf{B}_{\text{ND}}. \tag{29}$$

We have the following result.

Proposition 1. *The ND-stab scheme of Eq.* (28) *is unconditionally absolutely stable (and hence zero-stable) for any physically meaningful choice of parameters (that is $E \geq E_0$ for some $E_0 > 0$, $R > 0$, $C \geq 0$, $M \geq 0$).*

Proof. The non-zero eigenvalues of the Jacobian matrix $-\mathbf{A}_{\text{ND}-\text{stab}}^{-1}\mathbf{B}_{\text{ND}-\text{stab}}$ read (they can be obtained through symbolic computations)

$$\mu_{\pm} = \frac{2M + (C+R)\Delta t \pm \Delta t\sqrt{(C+R)^2 - 4EM}}{2(M + (C+R)\Delta t + E\Delta t^2)} = \frac{2M + \hat{C}\Delta t \pm \Delta t\sqrt{\hat{C}^2 - 4EM}}{2(M + \hat{C}\Delta t + E\Delta t^2)} \tag{30}$$

where we have defined $\hat{C} = C + R$. We consider two scenarios, depending on the sign of $\hat{C}^2 - 4EM$. Let us first suppose that $\hat{C}^2 \geq 4EM$. Then, we have

$$0 \leq \hat{C} \pm \sqrt{\hat{C}^2 - 4EM} \leq 2\hat{C},$$

which entails

$$0 \leq \frac{M}{M + \hat{C}\Delta t + E\Delta t^2} \leq \mu_{\pm} \leq \frac{M + \hat{C}\Delta t}{M + \hat{C}\Delta t + E\Delta t^2} < 1.$$

Consider now the case when $\hat{C}^2 < 4EM$. We have:

$$\mu_{\pm} = \frac{2M + \hat{C}\Delta t \pm i\Delta t\sqrt{4EM - \hat{C}^2}}{2(M + \hat{C}\Delta t + E\Delta t^2)},$$

which entails

$$\begin{aligned} |\mu_{\pm}|^2 &= \frac{(2M + \hat{C}\Delta t)^2 + \Delta t^2(4EM - \hat{C}^2)}{4(M + \hat{C}\Delta t + E\Delta t^2)^2} \\ &= \frac{M^2 + M\hat{C}\Delta t + EM\Delta t^2}{M^2 + \hat{C}^2\Delta t^2 + E^2\Delta t^4 + 2M\hat{C}\Delta t + 2ME\Delta t^2 + 2\hat{C}E\Delta t^3} < 1. \end{aligned}$$

The eigenvalues of the Jacobian matrix $-\mathbf{A}_{\mathrm{ND-stab}}^{-1}\mathbf{B}_{\mathrm{ND-stab}}$ are thus bounded in modulus by a constant strictly lower than 1. The thesis follows from Lemmas 1 and 2. □

In order to numerically verify the result of Prop. 1, in Fig. 10 we show the trend with respect to Δt of the spectrum of the Jacobian matrix $-\mathbf{A}^{-1}\mathbf{B}$ for the ND and ND-stab scheme, under different conditions (quasi-static case, with viscosity, with inertia and finally with both viscosity and inertia). The results show that, as expected, the ND-stab scheme has eigenvalues all less than one in modulus.

4.3 ND-stab scheme for a generic structure model

The ND-stab scheme, despite being derived for the minimal model of Eq. (28), can be generalized for a much wider class of models of FSI problems. We now show that the stability result of Prop. 1 can be extended to the generic structure mechanics model of Eq. (3), while still considering the minimal fluid model (12). Interestingly, in the proof we will formally reduce the generic model to the minimal one. Let us then consider the following FSI problem

$$\begin{cases} \mathcal{L}(\ddot{\mathbf{d}}(t), \dot{\mathbf{d}}(t), \mathbf{d}(t), p(t), t) = 0 & t > 0, \\ \dot{V}_{\mathcal{F}}(t) = Q_{\mathrm{valve}}(p_{\mathrm{ext}}(t) - p(t)) & t > 0, \\ V_{\mathcal{S}}(\mathbf{d}(t)) = V_{\mathcal{F}}(t) & t > 0, \\ \mathbf{d}(0) = \mathbf{d}_0,\ \dot{\mathbf{d}}(0) = \mathbf{0},\ V_{\mathcal{F}}(0) = V_0, \end{cases} \tag{31}$$

and the associated ND-stab scheme:

$$\begin{cases} \mathcal{L}\left(\dfrac{\mathbf{d}^{(k+1)} - 2\mathbf{d}^{(k)} + \mathbf{d}^{(k-1)}}{\Delta t^2}, \dfrac{\mathbf{d}^{(k+1)} - \mathbf{d}^{(k)}}{\Delta t}, \mathbf{d}^{(k+1)}, p^{(k+1)}, t_{k+1}\right) = 0 \quad k = 0, 1, \ldots \\ V_{\mathcal{S}}(\mathbf{d}^{(k+1)}) = V_{\mathcal{F}}^{(k)} + \Delta t\, Q_{\mathrm{stab}}(p^{(k+1)}, t_{k+1}) \qquad k = 0, 1, \ldots \\ \dfrac{V_{\mathcal{F}}^{(k+1)} - V_{\mathcal{F}}^{(k)}}{\Delta t} = Q_{\mathrm{valve}}(p_{\mathrm{ext}}(t_{k+1}) - p^{(k+1)}) \quad k = 0, 1, \ldots \end{cases} \tag{32}$$

We remark that problem (31) might arise from the Finite Element space discretization of virtually any nonlinear elastic or viscoelastic structure model. We then consider the following physically motivated assumptions.

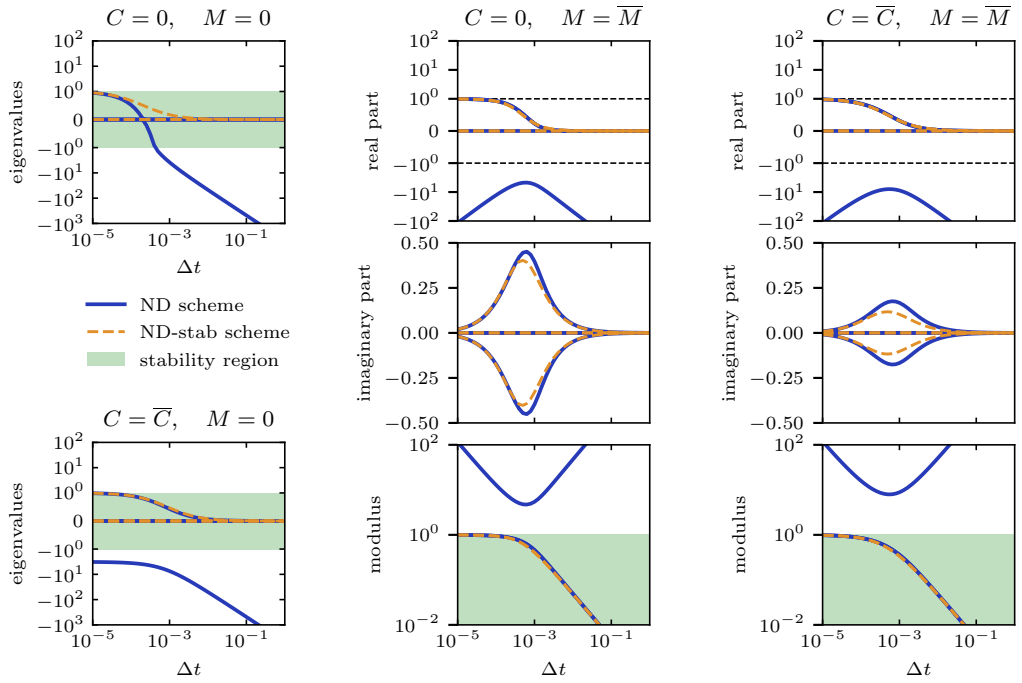

Figure 10: Eigenvalues of the Jacobian matrix $-\mathbf{A}^{-1}\mathbf{B}$ for the ND and ND-stab schemes in the open valve case ($R = R_{\min}$).

(A1) Let us define the mass matrix $\mathscr{M}$ and the damping matrix $\mathscr{C}$ as follows

$$\mathscr{M}(\ddot{\mathbf{d}}, \dot{\mathbf{d}}, \mathbf{d}, p, t) := \frac{\partial \mathcal{L}}{\partial \ddot{\mathbf{d}}}, \qquad \mathscr{C}(\ddot{\mathbf{d}}, \dot{\mathbf{d}}, \mathbf{d}, p, t) := \frac{\partial \mathcal{L}}{\partial \dot{\mathbf{d}}} .$$

We assume that both $\mathscr{M}$ and $\mathscr{C}$ has real nonnegative eigenvalues, bounded from above by $\lambda_{\mathscr{M}}^{\max} < +\infty$ and by $\lambda_{\mathscr{C}}^{\max} < +\infty$, respectively, uniformly with respect to the arguments. This assumption encompasses the case when inertia and/or damping are not included in the model ($\mathscr{M} = \mathscr{C} = \mathbb{O}$, the zero tensor).

(A2) Let us define the stiffness matrix

$$\mathscr{E}(\ddot{\mathbf{d}}, \dot{\mathbf{d}}, \mathbf{d}, p, t) := \frac{\partial \mathcal{L}}{\partial \mathbf{d}}. \tag{33}$$

We assume that $\mathscr{E}$ has real eigenvalues, bounded from below by $\lambda_{\mathscr{E}}^{\min} > 0$, uniformly with respect to its arguments. This assumption arises from thermodynamical requirements (ellipticity of the stiffness operator).

(A3) For physical consistency, we need the following relationship to hold true for any choice of $\ddot{\mathbf{d}}$, $\dot{\mathbf{d}}$, $\mathbf{d}$, p, t:

$$\frac{\partial \mathcal{L}}{\partial p} = -\frac{\partial V_{\mathcal{S}}}{\partial \mathbf{d}}.$$

This requirement derives from the principle of momentum conservation (see [42, 43]). In Prop. 2, we show that this holds true if, e.g., the boundary conditions of Eq. (2) are employed.

(A4) Let us define

$$R(p, t) := -\left(\frac{\partial Q_{\text{valve}}(p_{\text{ext}}(t) - p)}{\partial p}\right)^{-1}. \tag{34}$$

We assume that $0 < R(p, t) < R_{\max}$ for some $R_{\max} < +\infty$, uniformly with respect to p and t. This amounts to say that the valve has finite resistance, coherently with the valve model of Eq. (13).

The following proposition proves that Assumption (A3) holds true in case the boundary conditions of (2) are employed.

Proposition 2. *Suppose that the chamber volume is enclosed in the surface* Γ_0^{endo}. *Then, both Problem* (2) *and its Finite Element discretization satisfy Assumption (A3).*

Proof. As in Problem (31), we consider $N = 1$ cavities. The weak formulation of Problem (2) reads:

$$\int_{\Omega_0} \rho \frac{\partial^2 \mathbf{d}}{\partial t^2} \cdot \mathbf{v}\, dV_0 + \int_{\Omega_0} \mathbf{P}(\mathbf{d}, T_\mathrm{a}) \colon \nabla \mathbf{v}\, dV_0 + \int_{\Gamma_0^{\text{endo}}} p\, J\mathbf{F}^{-T}\mathbf{N} \cdot \mathbf{v}\, dS_0 = 0 \qquad \forall \mathbf{v} \in V := [H^1(\Omega_0)]^3.$$

Notice that additional terms could be present for other portions of the boundary, but this would not affect the result. It follows that, for any $\mathbf{v} \in V$:

$$\langle \frac{\partial \mathcal{L}}{\partial p}, \mathbf{v} \rangle = \int_{\Gamma_0^{\text{endo}}} J\mathbf{F}^{-T}\mathbf{N} \cdot \mathbf{v}\, dS_0,$$

where $\langle \cdot, \cdot \rangle$ denotes the duality pairing between V and its dual V^*.

Let us denote by Ω_0^{f} the volume enclosed into Γ_0^{endo}. Moreover, we denote by $\Gamma^{\text{endo}}(\mathbf{d})$ the result of deforming the surface Γ_0^{endo} according to the displacement field $\mathbf{d}$, and by $\Omega^{\mathrm{f}}(\mathbf{d})$ the enclosed volume. We denote by $\mathbf{n}$ the unit vector, normal to the surface $\Gamma^{\text{endo}}(\mathbf{d})$ in the current configuration, directed from the solid to the fluid domain. The fluid volume function then reads:

$$V_{\mathcal{S}}(\mathbf{d}) = \int_{\Omega^{\mathrm{f}}(\mathbf{d})} 1\, dV_t = \int_{\Omega_0^{\mathrm{f}}} J\, dV_0.$$

By Reynolds transport theorem [21], the Gateaux derivative of the volume reads, for any $\mathbf{v} \in V$

$$\langle \frac{\partial V_{\mathcal{S}}}{\partial \mathbf{d}}, \mathbf{v} \rangle = -\int_{\Gamma^{\text{endo}}(\mathbf{d})} \mathbf{v} \cdot \mathbf{n}\, dS_t = -\int_{\Gamma_0^{\text{endo}}} J\mathbf{F}^{-T}\mathbf{N} \cdot \mathbf{v}\, dS_0,$$

where we have computed the pull-back in the reference configuration. This proves Assumption (A3). To prove the discrete case, it is sufficient to take as $\mathbf{v}$ the elements of the base of the Finite Element space. □

We have the following stability result for the ND-stab scheme, that extends Prop. 1 to a generic structure model.

Proposition 3. *Let us consider problem* (31)*, with assumtions (A1)–(A2)–(A3)–(A4). The ND-stab scheme of Eq.* (32) *is unconditionally absolutely stable (and hence zero-stable).*

Proof. The scheme (32) belongs to the abstract family (17), provided that we define the state vector $\boldsymbol{\psi}^{(k)} := (\mathbf{d}^{(k)}, \mathbf{d}^{(k-1)}, V_{\mathcal{F}}^{(k)}, p^{(k)})^T$. With reference to Lemmas 1 and 2, we have

$$\mathbf{A} = \begin{pmatrix} \mathscr{E} + \frac{\mathscr{M}}{\Delta t^2} + \frac{\mathscr{C}}{\Delta t} & -\frac{\mathscr{M}}{\Delta t^2} & \mathbf{0} & -\mathbf{r} \\ \mathbb{O} & \mathbb{I} & \mathbf{0} & \mathbf{0} \\ \mathbf{0}^T & \mathbf{0}^T & \Delta t^{-1} & R^{-1} \\ \mathbf{r}^T & \mathbf{0}^T & 0 & \frac{\Delta t}{R} \end{pmatrix}, \quad \mathbf{B} = \begin{pmatrix} -\left(\frac{\mathscr{M}}{\Delta t^2} + \frac{\mathscr{C}}{\Delta t}\right) & \frac{\mathscr{M}}{\Delta t^2} & \mathbf{0} & \mathbf{0} \\ -\mathbb{I} & \mathbb{O} & \mathbf{0} & \mathbf{0} \\ \mathbf{0}^T & \mathbf{0}^T & -\Delta t^{-1} & 0 \\ \mathbf{0}^T & \mathbf{0}^T & -1 & 0 \end{pmatrix}. \tag{35}$$

where we have defined $\mathbf{r} := \frac{\partial V_{\mathcal{S}}}{\partial \mathbf{d}}$ and where the dependence on the arguments is understood. We denote by $\mathbb{I}$ and $\mathbb{O}$ the identity and zero matrices, respectively. We consider the generalized eigenvalues problem $\mu\mathbf{A}\boldsymbol{\psi} + \mathbf{B}\boldsymbol{\psi} = \mathbf{0}$, for $\boldsymbol{\psi} \neq \mathbf{0}$ and we look for nonnegative eigenvalues $\mu \neq 0$. By writing the eigenvector as $\boldsymbol{\psi} = (\hat{\mathbf{d}}, \mathbf{d}, V_{\mathcal{F}}, p)^T$, each eigenvalue-eigenvector pair solves

$$\frac{\mu^2 - 2\mu + 1}{\Delta t^2}\mathscr{M}\mathbf{d} + \frac{\mu^2 - \mu}{\Delta t}\mathscr{C}\mathbf{d} + \mathscr{E}\mathbf{d} = \mu p \mathbf{r} \tag{36a}$$

$$\frac{\mu - 1}{\Delta t} V_{\mathcal{F}} = -\frac{\mu p}{R} \tag{36b}$$

$$\mu^2 \mathbf{r}^T \mathbf{d} = V_{\mathcal{F}} - \frac{\Delta t}{R}\mu p \tag{36c}$$

We first consider the case when $\mathbf{d} = \mathbf{0}$. From (36b) and (36c), it follows $V_{\mathcal{F}} = 0$ and hence, by using again (36b), $p = 0$. Thus we get $\boldsymbol{\psi} = \mathbf{0}$ that is not a valid eigenvector. Therefore, from now on we assume $\mathbf{d} \neq \mathbf{0}$. From (36b) and (36c) it follows $V_{\mathcal{F}} = \mu \mathbf{r}^T \mathbf{d}$ and hence $p = \frac{R}{\Delta t}(1-\mu)\mathbf{r}^T\mathbf{d}$. Replacing this into (36a), we have:

$$\left(\frac{\mu^2 - 2\mu + 1}{\Delta t^2} \mathscr{M} + \frac{\mu^2 - \mu}{\Delta t} (\mathscr{C} + R\mathbf{r}\mathbf{r}^T) + \mathscr{E} \right) \mathbf{d} = \mathbf{0}. \tag{37}$$

We left multiply (37) by the Hermitian transpose of $\mathbf{d}$, thus getting

$$\frac{\mu^2 - 2\mu + 1}{\Delta t^2} \hat{M} + \frac{\mu^2 - \mu}{\Delta t} \hat{C} + \hat{E} = 0, \tag{38}$$

where we have defined

$$\hat{M} = \frac{\mathbf{d}^H \mathscr{M} \mathbf{d}}{\mathbf{d}^H \mathbf{d}}, \quad \hat{C} = \frac{\mathbf{d}^H (\mathscr{C} + R\mathbf{r}\mathbf{r}^T)\mathbf{d}}{\mathbf{d}^H \mathbf{d}}, \quad \hat{E} = \frac{\mathbf{d}^H \mathscr{E} \mathbf{d}}{\mathbf{d}^H \mathbf{d}}$$

Assumptions (A1) and (A4) entail $0 \leq \hat{M} \leq \lambda_{\mathscr{M}}^{\max}$ and $0 \leq \hat{C} \leq \lambda_{\mathscr{C}}^{\max} + R_{\max}\|\mathbf{r}\|^2$. Moreover, by assumption (A2) we have $\hat{E} \leq \lambda_{\mathscr{E}}^{\min}$. From Eq. (38) it follows that two eigenvalues are possible, according to

$$\mu_{\pm} = \frac{2\hat{M} + \hat{C}\Delta t \pm \Delta t \sqrt{\hat{C}^2 - 4\hat{E}\hat{M}}}{2(\hat{M} + \hat{C}\Delta t + \hat{E}\Delta t^2)}.$$

We have thus formally recovered the minimal model of Prop. 1 (see Eq. (30)). Therefore, by proceeding as in the proof of Prop. 1, we have

$$|\mu_{\pm}| \leq \frac{\hat{M} + \hat{C}\Delta t}{\hat{M} + \hat{C}\Delta t + \hat{E}\Delta t^2}, \tag{39}$$

if $\hat{C}^2 \geq 4\hat{E}\hat{M}$; otherwise, we have

$$|\mu_{\pm}|^2 = \frac{\hat{M}^2 + \hat{M}\hat{C}\Delta t + \hat{E}\hat{M}\Delta t^2}{\hat{M}^2 + \hat{C}^2\Delta t^2 + \hat{E}^2\Delta t^4 + 2\hat{M}\hat{C}\Delta t + 2\hat{M}\hat{E}\Delta t^2 + 2\hat{C}\hat{E}\Delta t^3}. \tag{40}$$

In both cases, the eigenvalues have modulus strictly lower than one. This proves zero-stability. To prove absolute stability, instead, we need to show that the eigenvalues modulus is bounded by a constant strictly lower than 1, uniformly with respect to the state $\boldsymbol{\psi}$. This is proved by the fact that both the right-hand sides of Eqs. (39) and (40) are non-increasing in $\hat{E}$, which is bounded from below by $\lambda_{\mathscr{E}}^{\min}$, and by the fact that they are continuous in $(\hat{M}, \hat{C})$, which belongs to the compact set $[0, \lambda_{\mathscr{M}}^{\max}] \times [0, \lambda_{\mathscr{C}}^{\max} + R_{\max}\|\mathbf{r}\|^2]$. □

Finally, we show how the ND-stab scheme, that we proposed on the minimal model (12), can be generalized to more complex fluid models. The vector collecting the net blood fluxes associated with the N, as predicetd by the fluid model, is given by

$$\frac{d\mathbf{V}_{\mathcal{F}}(\mathbf{c}(t))}{dt} = \frac{\partial \mathbf{V}_{\mathcal{F}}(\mathbf{c}(t))}{\partial \mathbf{c}} \mathbf{H}(\mathbf{c}(t), \mathbf{p}(t), t).$$

Therefore, we define the flux function

$$\mathbf{Q}_{\text{stab}}(\mathbf{p}, \mathbf{c}, t) = \frac{\partial \mathbf{V}_{\mathcal{F}}(\mathbf{c})}{\partial \mathbf{c}} \mathbf{H}(\mathbf{c}, \mathbf{p}, t).$$

The ND-stab scheme then reads

$$\begin{cases} \mathcal{L}\left(\dfrac{\mathbf{d}^{(k+1)} - 2\mathbf{d}^{(k)} + \mathbf{d}^{(k-1)}}{\Delta t^2}, \dfrac{\mathbf{d}^{(k+1)} - \mathbf{d}^{(k)}}{\Delta t}, \mathbf{d}^{(k+1)}, \mathbf{p}^{(k+1)}, t_{k+1} \right) = 0 \quad k = 0, 1, \dots \\ \mathbf{V}_{\mathcal{S}}(\mathbf{d}^{(k+1)}) = \mathbf{V}_{\mathcal{F}}(\mathbf{c}^{(k)}) + \Delta t\, \mathbf{Q}_{\text{stab}}(\mathbf{p}^{(k+1)}, \mathbf{c}^{(k)}, t_{k+1}) \qquad k = 0, 1, \dots \\ \dfrac{\mathbf{c}^{(k+1)} - \mathbf{c}^{(k)}}{\Delta t} = \mathbf{H}\left(\mathbf{c}^{(\star)}, \mathbf{p}^{(k+1)}, t_{k+1} \right) \quad k = 0, 1, \dots \end{cases} \tag{41}$$

For this case we do not provide a theoretical result, but will show numerical evidence of the effectiveness of the stabilization term in Sec. 5.

We notice that, unlike for the ND scheme of Eq. (9), for the ND-stab scheme the pressures $\mathbf{p}^{(k+1)}$ also account as unknowns in the second equation of the structure mechanics substep of the ND-stab scheme of Eq. (41). The numerical resolution of the structure mechanics substep can be efficiently performed through the Newton method. In Appendix C we report an efficient algorithm, based on a Schur complement reduction, for solving the linear system associated with each Newton iteration.

5 Results

In this section, we present and discuss some numerical tests aimed at verifying the theoretical results presented in this paper and the effectiveness of the proposed method. First, in Sec. 5.1, we consider the minimal model introduced in Sec. 3.1. Then, in Sec. 5.2, we consider the application of the ND-stab scheme to a multi-scale left ventricular model of cardiac electromechanics.

5.1 Minimal model

We consider the minimal model of Eq. (14) (see also Fig. 1a). To demonstrate the generality of the results of Secs. 3 and 4, that is valid for both linear and nonlinear models, we consider a nonlinear law for the passive constitutive behavior of the cardiac chamber. Specifically, we consider the Klotz's law [26]:

$$p_{\text{pass}}(V) = A_n \left(\frac{V - V_0^{\text{klotz}}}{V_{30}^{\text{klotz}} - V_0^{\text{klotz}}} \right)^{B_n}, \tag{42}$$

with $V_0^{\text{klotz}} = 10\,\text{mL}$, $V_{30}^{\text{klotz}} = 170\,\text{mL}$, $A_n = 28.2\,\text{mmHg}$ and $B_n = 2.79$. We consider the parameters reported in Tab. 1 with no active tension ($T_{\text{a}}(t) \equiv 0$). Moreover, we consider the case of an inflow cardiac valve (i.e. $Q_{\text{valve}} = Q_{\text{valve}}^{\text{in}}$). We run the simulation until time $T = 0.2\,\text{s}$, starting with a volume $V_0 = 120\,\text{mL}$ and imposing the following external pressure transient:

$$p_{\text{ext}}(t) = p_{\min} + (p_{\max} - p_{\min}) \sin\left(\frac{\pi\, t}{T}\right),$$

with $p_{\min} = 5\,\text{mmHg}$ and $p_{\max} = 20\,\text{mmHg}$.

In this test case, the pressure inside the cardiac chamber at time $t = 0$ is $p(0) = 10\,\text{mmHg}$. The valve is therefore closed (negative pressure gradient: $p_{\text{ext}}(t) - p(t) < 0$) and the chamber volume is almost constant in time. Then, approximately at $t = 0.03\,\text{s}$, the external pressure $p_{\text{ext}}(t)$ exceeds the internal pressure $p(t)$. Consequently, the valve opens and blood begins to flow into the chamber, causing an increase in fluid volume. Finally, the sign of the pressure gradient reverses again and the valve closes, causing the volume to become constant in time.

5.1.1 Numerical simulations

In order to numerically verify the results of Secs. 3 and 4, we perform several numerical simulations of the model described above, for different time step sizes and by comparing the ND and the ND-stab schemes. In each test, we superimpose the obtained numerical solutions with a reference solution, obtained by means of a monolithic scheme and with a very small time step size ($\Delta t = 10^{-6}\,\text{s}$).

First, we consider the case when viscosity is present ($C \neq 0$), while inertia is neglected ($M = 0$). The analysis of Sec. 3 predicts that the ND scheme is never absolutely stable for $C = \overline{C}$ (see Fig. 5). This is verified by our numerical results. In fact, the solution of the ND scheme exhibits nonphysical pressure oscillations throughout the duration of the open valve phase (see first two columns of Fig. 11). Moreover, as expected, when the valve is closed the oscillations are not present. Coherently with the predictions, these oscillations are not cured even by decreasing the time step size. Instead, the amplitude of the oscillations remains constant (this is due to the fact that the negative eigenvalue has a horizontal asymptote for $\Delta t \to 0^+$, see Fig. 5). On the other hand, by decreasing the viscosity coefficient (in particular for $C = 0.1\,\overline{C}$) the ND scheme becomes absolutely stable for any choice of Δt (see Fig. 5).

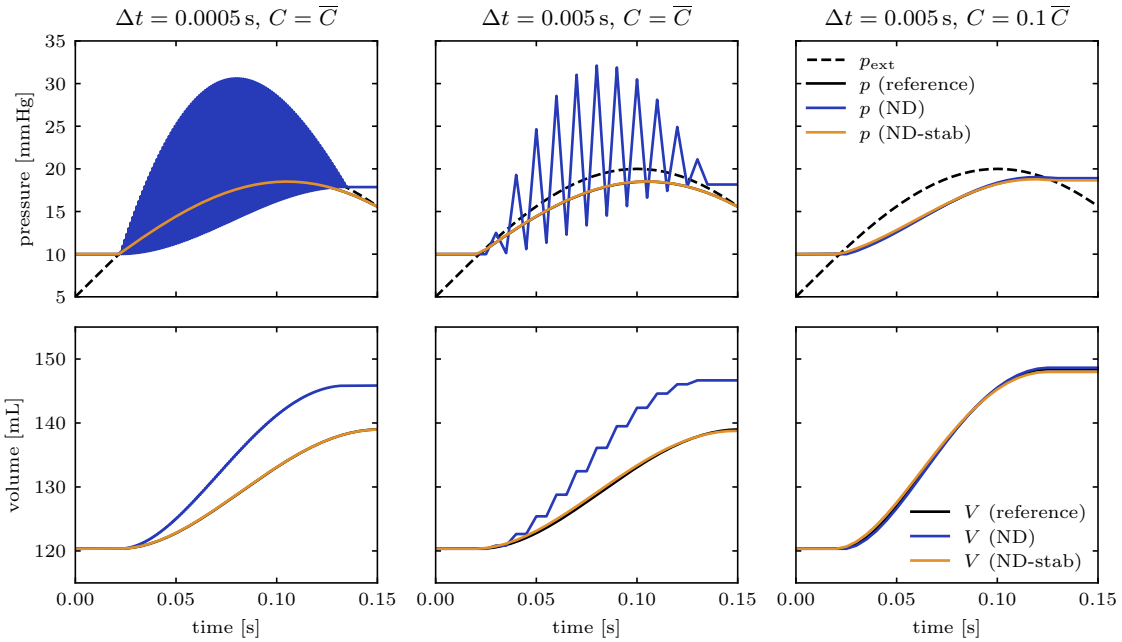

Figure 11: Results of numerical simulations of the model of Sec. 5.1, in the case when viscosity is present ($C \neq 0$), while inertia is neglected ($M = 0$). The values of C and Δt are reported in the titles. We compare the results obtained with the ND scheme, the ND-stab scheme and the reference solution.

Our results also confirm this prediction (see e.g. the third column of Fig. 11 for the case $\Delta t = 5 \cdot 10^{-3}\,\mathrm{s}$). On the other hand, in all the considered cases, our proposed ND-stab scheme does not present numerical oscillations and the solution is close to the reference one.

The predictions of Sec. 3 are also verified in the case with inertia and without viscosity ($M \neq 0$, $C = 0$), as shown in Fig. 12. Indeed, according to the stability analysis considered in Fig. 6, for $\Delta t = 5 \cdot 10^{-3}\,\mathrm{s}$ the ND scheme is absolutely stable. On the other hand, when $\Delta t \to 0^+$ numerical oscillations show up, with increasing amplitude (the eigenvalue responsible for the oscillations indeed blows up when $\Delta t \to 0^+$). Also in this case, the ND-stab successfully cures the nonphysical oscillations.

Finally, in Fig. 13 we consider the case when both viscosity and inertia are included in the model. Also in this case, the ND scheme exhibits the nonphysical oscillations predicted by the spectral analysis considered in Fig. 7, while the ND-stab scheme yields a stable solution, that is close to the reference one.

5.1.2 Convergence test

The ND-stab scheme introduces, in the ND scheme, a numerically consistent stabilization term of first order (see Sec. 4.1), $\mathcal{O}(\Delta t)$, when $\Delta t \to 0^+$. Since the numerical scheme of time advancement is also of first order, we expect the ND-stab scheme to be convergent of order 1 with respect to Δt (see e.g. [39]).

To numerically verify what said above, we solve the model of Sec. 5.1 by the ND-stab scheme, progressively halving the time step size Δt, from $2^{-5}\,\mathrm{s}$ to $2^{-14}\,\mathrm{s}$. We then plot the trend of the errors obtained against a reference solution, achieved via a monolithic scheme for $\Delta t = 2^{-20}\,\mathrm{s} \simeq 10^{-6}\,\mathrm{s}$. For simplicity, we only consider the case with both viscosity and inertia. In Fig. 14 we show that both the $L^2(0,T)$ and the $L^\infty(0,T)$ errors follow the expected first order trend with respect to Δt, both for the pressure and for the volume solution.

5.2 Multiscale cardiac electromechanics

We now apply the ND-stab scheme to a multiscale simulation of cardiac electromechanics. We employ the cardiac model proposed in [43], that we briefly recall in Secs. 5.2.1 and 5.2.2. Still, we remark that the

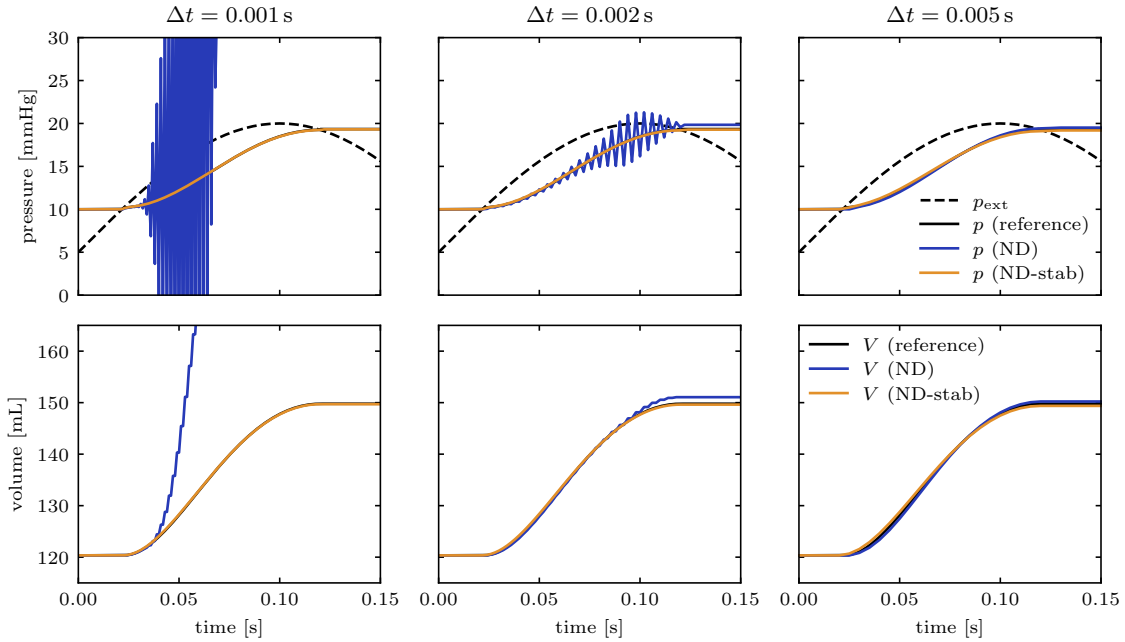

Figure 12: Results of numerical simulations of the model of Sec. 5.1, in the case when inertia is present ($M = \overline{M}$), while viscosity is neglected ($C = 0$). The values of Δt are reported in the titles. We compare the results obtained with the ND scheme, the ND-stab scheme and the reference solution.

ND-stab scheme proposed in this paper can be applied to any coupled mechanics-hemodynamics model in the form of Eq. (6).

5.2.1 The electromechanical model

We consider a realistic left-ventricular geometry, processed from the Zygote 3D heart model [53] by exploiting the semi-automatic meshing tool proposed in [12] (see Fig. 15b). The geometry is further processed through the algorithm proposed in [43] to recover the unloaded reference configuration. To generate the cardiac fibers, we adopt the Bayer-Blake-Plank-Trayanova algorithm [6]. Cardiac muscle contraction is driven by an electrical signal that propagates throughout the myocardium, thereby causing muscle tissue to contract. To model these processes, we adopt the monodomain equation [9], the *ten Tusscher-Panfilov* ionic model [49] and the RDQ20-MF model [41] of microscale force generation. Tissue mechanics is described through Eq. (2), where for the hyperelastic energy functional $\mathcal{W}$ we adopt the quasi-incompressible exponential constitutive law of [51]. To model the interaction of the ventricle with the pericardium, we employ spring-damper boundary conditions, while to model the interaction with the part of the myocardium above the artificial ventricular base, we adopt energy-consistent boundary conditions [42]. More precisely, we complement Eq. (2) with the following boundary conditions

$$\begin{cases} \mathbf{P}(\mathbf{d}, T_{\mathrm{a}})\mathbf{N} = \left[K_{\perp}^{\mathrm{epi}}(\mathbf{N}\otimes\mathbf{N}) + K_{\parallel}^{\mathrm{epi}}(\mathbf{I}-\mathbf{N}\otimes\mathbf{N})\right]\mathbf{d} \\ \qquad\qquad + \left[C_{\perp}^{\mathrm{epi}}(\mathbf{N}\otimes\mathbf{N}) + C_{\parallel}^{\mathrm{epi}}(\mathbf{I}-\mathbf{N}\otimes\mathbf{N})\right]\dfrac{\partial \mathbf{d}}{\partial t}, \quad \text{on } \Gamma_0^{\mathrm{epi}}\times(0,T), \\ \mathbf{P}(\mathbf{d}, T_{\mathrm{a}})\mathbf{N} = p\,|J\mathbf{F}^{-T}\mathbf{N}|\,\dfrac{\int_{\Gamma_0^{\mathrm{endo}}} J\mathbf{F}^{-T}\mathbf{N}d\Gamma_0}{\int_{\Gamma_0^{\mathrm{base}}}|J\mathbf{F}^{-T}\mathbf{N}|d\Gamma_0}, \qquad \text{on } \Gamma_0^{\mathrm{base}}\times(0,T), \end{cases} \tag{43}$$

where the constants $K_{\perp}^{\mathrm{epi}}$, $K_{\parallel}^{\mathrm{epi}}$, $C_{\perp}^{\mathrm{epi}}$, $C_{\parallel}^{\mathrm{epi}} \in \mathbb{R}^+$ are associated with the stiffness and the viscosity of the tissue surrounding the epicardium in the normal or tangential directions, respectively, and where we denote by p the left ventricle blood pressure.

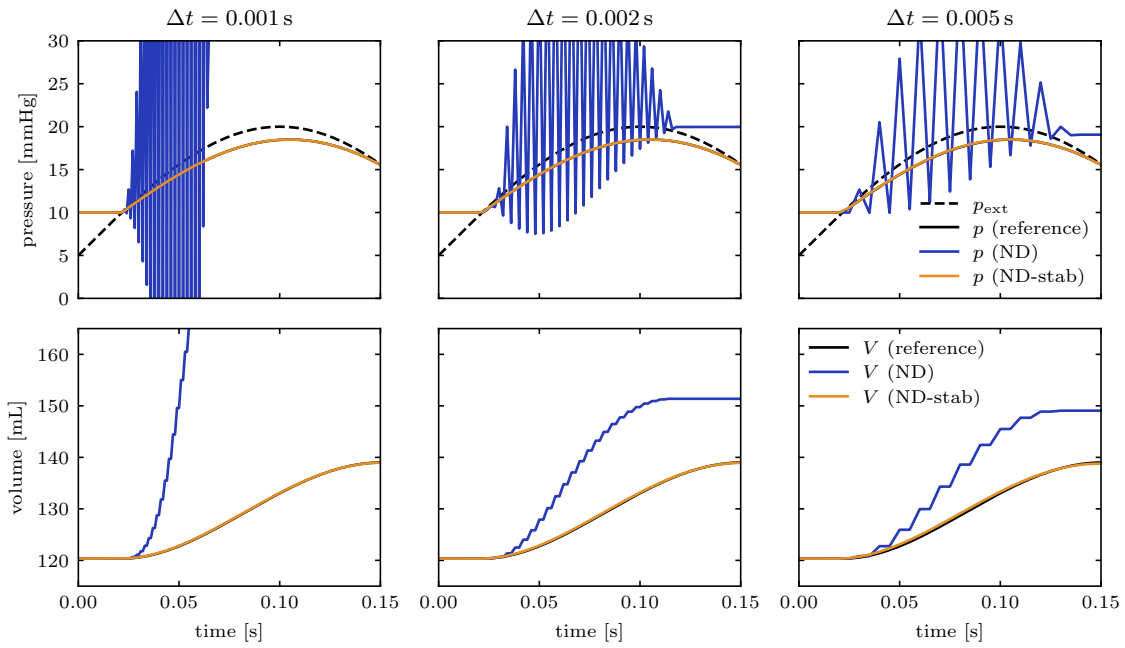

Figure 13: Results of numerical simulations of the model of Sec. 5.1, in the case when both inertia and viscosity are present ($C = \overline{C}$, $M = \overline{M}$). The values of Δt are reported in the titles. We compare the results obtained with the ND scheme, the ND-stab scheme and the reference solution.

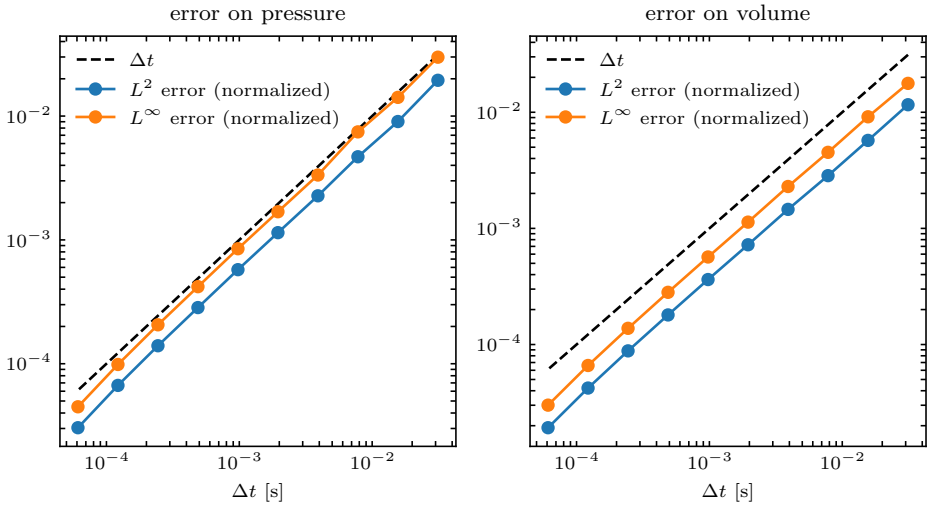

Figure 14: Error trend on the numerical solution obtained by means of the ND-scheme for the model of Sec. 5.1.

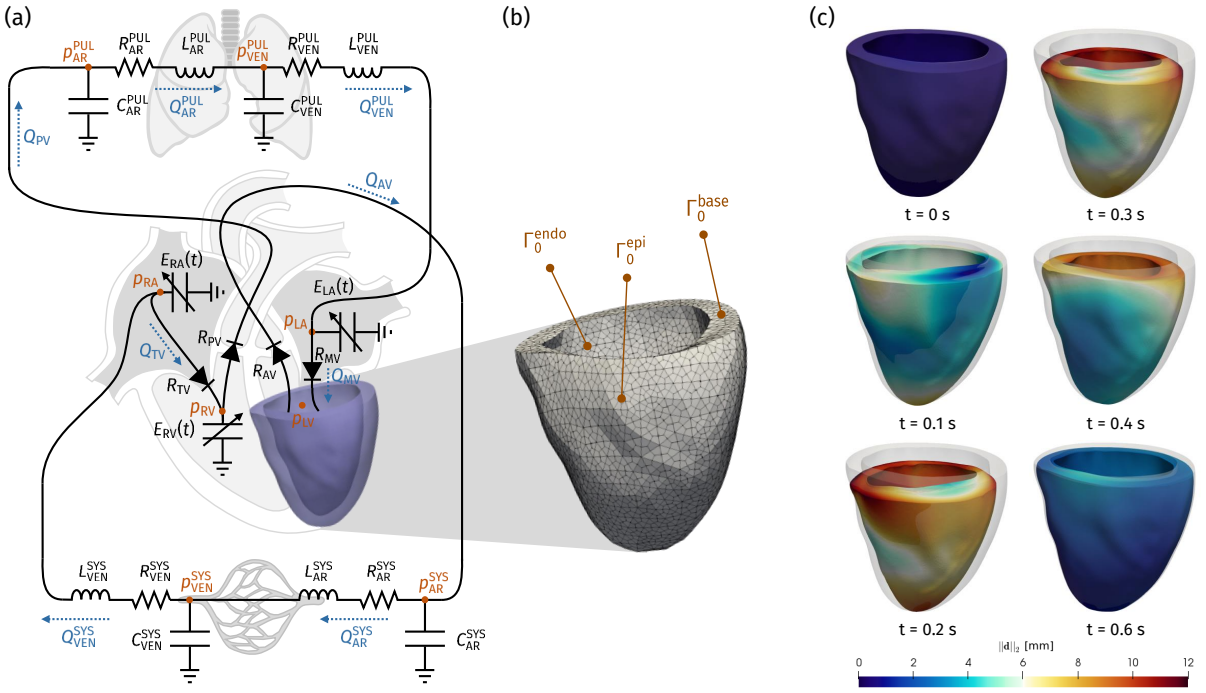

Figure 15: The multiscale coupled mechanics-hemodynamics model of Sec. 5.2 (a); computational mesh and boundary tags (b); snapshots of the numerical solution at selected time instants showing the tissue displacement (c).

To model blood circulation (model $\mathcal{F}$), we adopt the closed-loop lumped-parameter model of [43]. This model is based on a compartmental description of the systemic and pulmonary, arterial and venous circulatory networks (modeled as resistance-inductance-capacitance circuits), the four cardiac chambers (modeled by means of time-varying elastance models) and the four valves (modeled as diodes, as in Eq. 13). The coupled 0D-3D FSI model is represented in Fig. 15a, while in Fig. 15c, the numerically obtained tissue displacement is displayed at selected time instants. More details on the employed mathematical models and their coupling can be found in [43].

5.2.2 Numerical approximation

For the numerical approximation of the multiscale left ventricular model (model $\mathcal{S}$), we employ bilinear Finite Elements defined on two nested hexahedral meshes (a finer one for the electrophysiological variables and a coarser one for the structure mechanics variables). For the time integration of this multiphysics model we employ the staggered approach proposed in [43], that envisages – at each time step – a sequential update of the ionic variables, the electrical potential, the activation variables and finally the tissue displacement. For the time integration of the circulation model (model $\mathcal{F}$), we employ a Forward Euler scheme.

Concerning the coupling between the model $\mathcal{S}$ and the model $\mathcal{F}$, we compare the ND scheme with the ND-stab scheme (see Eq. (9) and Eq. (41), respectively).

5.2.3 Comparison of ND and ND-stab schemes

In Fig. 16 we show the transients of pressures, volumes, and blood fluxes obtained using the ND and ND-stab schemes for the numerical approximation of the multiscale model of cardiac electromechanics and hemodynamics described in Sec. 5.2.1.

On the one hand, we notice that the solution obtained using the ND scheme presents numerical oscillations in two phases of the heartbeat. Both of these episodes occur when at least one valve is open

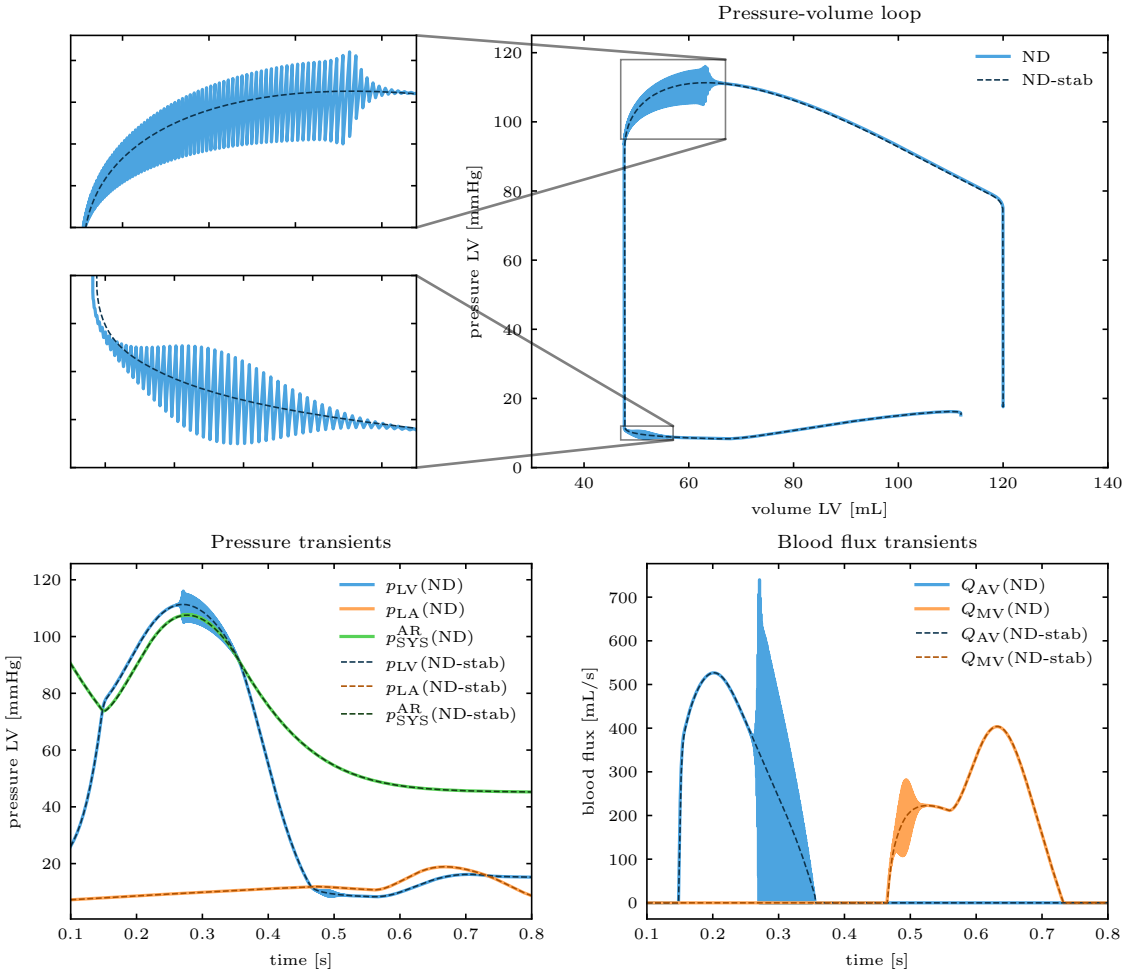

Figure 16: Numerical solution of pressures, volume and blood fluxes of the multiscale model of cardiac electromechanics of Sec. 5.2: comparison between ND and ND-stab schemes. Top: pressure volume loop. Bottom left: pressure transients associated with the left ventricle (p_{LV}), the left atrium (p_{LA}) and the systemic arterial circulation ($p^{\mathrm{SYS}}_{\mathrm{AR}}$). Bottom right: blood fluxes across the aortic valve (Q_{AV}) and the mitral valve (Q_{MV}).

(in one case the aortic valve, in the other case the mitral valve). This is in line with the results of Sec. 3, which show that the ND scheme features instability issues mainly when the resistance between the chamber and the external circulation is low, i.e. when one valve is open.

On the other hand, the stabilization term introduced by the ND-stab scheme proposed in this paper is able to successfully remove the non-physical oscillations that would otherwise affect the volume and pressure transients, as well as the tissue displacement and the computed stress.

6 Conclusions

In this paper we investigated the numerical stability of staggered schemes for 0D-3D FSI problems. We focused on a problem of great applicative interest, that is the interaction between 3D models of cardiac mechanics and 0D models of blood dynamics. We considered two schemes: the Dirichlet-Neumann (DN) scheme, in which pressures are updated simultaneously with the variables of the fluid model, and the Neumann-Dirichlet (ND) scheme, in which pressures are determined simultaneously with the displacement

of the structure mechanics model.

We provided analytical results on the numerical stability of these schemes. We showed that the DN scheme suffers from severe instability issues in case of an incompressible fluid enclosed in a cavity (e.g., during isovolumetric phases of an heartbeat). This is related to the so-called balloon dilemma [5, 20], for which we provided an algebraic interpretation in terms of an eigenvalue of the Jacobian matrix that tends to $-\infty$ when the closed valve resistance increases, thus approaching the incompressible limit. The ND scheme, instead, is numerically stable when the valves are closed but might exhibit nonphysical oscillations when at least one valve is open (that is, with a non negligible fluid flow). The onset of these numerical oscillations is associated with the following features of the model at hand.

- *Stiffness of the structure.* A stiff tissue (equivalently, a large elastance) promotes the onset of oscillations. For parameters values typical of cardiac models, however, stiffness per se imposes very mild limits on Δt (nearly $\Delta t < 10^{-1}$ s).
- *Viscosity.* When the structure mechanics model features a large energy dissipation (either due to viscous boundary conditions or to a visco-elastic structure mechanics model), the ND scheme is numerically unstable. In this case, reducing Δt does not cure the numerical instabilities.
- *Inertia.* Similarly to viscosity, a large inertia makes the ND scheme unstable. Moreover, when inertial effects are included in the structure mechanics model, for small enough Δt the ND scheme features an eigenvalue lower than -1 and the scheme is numerically unstable. In conclusion, the ND scheme is never zero-stable when inertia is present and consequently is never convergent.
- *Active stress model with velocity dependence.* When dealing with active materials, and specifically when using a cardiac force generation model that accounts for fiber shortening velocity feedback on active force, the ND scheme may suffer from numerical instabilities. In particular, when the tissue is highly activated (typically in systole), crossbridge stiffness at the microscopic level has the effect, at the macroscopic level, of an increase in the effective stiffness (the increase can be up to 400-fold). This brings us back to the first point in this list, but with much more severe limits on Δt.

We then introduced a numerically consistent stabilization term that is able to prevent the onset of numerical oscillations in the ND scheme. We have shown that the stabilized ND scheme (ND-stab scheme) is absolutely stable for any choice of Δt and of model parameters. From the implementation point of view, this stabilization term requires only a small modification with respect to the ND scheme. In addition, we proposed an effective algorithm, based on a Schur complement reduction, for solving the linear system that emerges at each Newton iteration when advancing the structure mechanics model. Our scheme requires solving $N + 1$ linear systems (N being the number of cavities considered in the model), where the matrix is the Jacobian of the standalone structure mechanics model, thus allowing reusing pre-existing solvers and preconditioners.

Our numerical simulations confirmed the theoretical results mentioned above. Specifically, we showed simulations obtained with a minimal FSI model, performing numerical tests under different conditions and verifying the expected order of convergence with respect to Δt. Then, we showed a simulation obtained with a multiscale model of cardiac electromechanics in a left ventricle, coupled with a lumped-parameter closed-loop model of the circulatory system. All the cases described above confirm that the stabilization term proposed in this paper is successful in removing the nonphysical oscillations, for any choice of parameters and for any value of Δt.

Appendix A Derivation of the minimal model

In this appendix, we present the derivation of the minimal model of left ventricle mechanics of Eq. (11), starting from the 3D model of Eqs. (2) and (43). More precisely, the derivation of the minimal model is based on the energy balance stemming from the 3D model. As demonstrated in [42, 43] – by multiplying the first equation of Eq. (2) by $\frac{\partial \mathbf{d}}{\partial t}$, integrating over Ω_0 and accounting for the boundary conditions – we have:

$$\frac{d}{dt}\mathcal{K}(t) + \frac{d}{dt}\mathcal{E}(t) = \Pi^{\text{act}}(t) + \Pi^{\text{diss}}(t) + \Pi^{\text{press}}(t), \tag{44}$$

that is a balance between the rate of change of the total kinetic ($\mathcal{K}$) and potential ($\mathcal{E}$) energy and the power associated with active forces (Π^{act}), viscous dissipation (Π^{diss}) and blood pressure (Π^{press}), defined as

$$\begin{aligned}
&\mathcal{E}(t) = \int_{\Omega_0} \mathcal{W}(\mathbf{F}) d\mathbf{x} + \frac{1}{2}\int_{\Gamma_0^{\text{epi}}} \left[K_\perp^{\text{epi}} \left|\mathbf{d}\cdot\mathbf{N}\right|^2 + K_\parallel^{\text{epi}} \left|(\mathbf{I}-\mathbf{N}\otimes\mathbf{N})\mathbf{d}\right|^2\right] d\Gamma_0,\\
&\mathcal{K}(t) = \frac{1}{2}\int_{\Omega_0} \rho \left|\frac{\partial \mathbf{d}}{\partial t}\right|^2 d\mathbf{x}, \qquad \Pi^{\text{act}}(t) = -\int_{\Omega_0} T_{\text{a}} \frac{\mathbf{F}\mathbf{f}_0\otimes\mathbf{f}_0}{\sqrt{\mathcal{I}_{4f}}} : \nabla\left(\frac{\partial \mathbf{d}}{\partial t}\right) d\mathbf{x},\\
&\Pi^{\text{diss}}(t) = -\int_{\Gamma_0^{\text{epi}}} \left[C_\perp^{\text{epi}} \left|\frac{\partial \mathbf{d}}{\partial t}\cdot\mathbf{N}\right|^2 + C_\parallel^{\text{epi}} \left|(\mathbf{I}-\mathbf{N}\otimes\mathbf{N})\frac{\partial \mathbf{d}}{\partial t}\right|^2\right] d\Gamma_0,\\
&\Pi^{\text{press}}(t) = p(t)\tfrac{d}{dt}V(\mathbf{d}(t)).
\end{aligned}$$

where p and V represent the pressure and volume of the blood contained in the left ventricle.

To derive a lumped-parameter model for the left ventricle dynamics, we consider the volume V as a state variable, and we express the terms of Eq. (44) as functions of V and its time derivatives, making suitable approximations where needed.

First, by assuming that the potential energy is function of the state variable V, we have $\mathcal{E}(t) = \widetilde{\mathcal{E}}(V(t))$ for some function $\widetilde{\mathcal{E}}$. We accordingly define the steady-state pressure corresponding to a non activated tissue as $p_{\text{pass}}(V) := \widetilde{\mathcal{E}}'(V)$.

Then, we assume that the inertial and damping effects are mainly associated with the tissue motion in radial direction. We then consider a displacement of the form of $\mathbf{d}(\mathbf{x},t) = (r(t)-r_0)\mathbf{e}_\rho(\mathbf{x})$, where $\mathbf{e}_\rho$ is the radial unit vector, having set without loss of generality the origin in the barycenter of Ω_0. It follows:

$$\mathcal{K}(t) \simeq \frac{1}{2}\left[\int_{\Omega_0} \rho\, d\mathbf{x}\right] \dot{r}^2(t) = \frac{1}{2} M_{\text{LV}}\, \dot{r}^2(t), \qquad \Pi^{\text{diss}}(t) \simeq -C_\perp^{\text{epi}} |\Gamma_0^{\text{epi}}| \dot{r}^2(t) \tag{45}$$

where M_{LV} denotes the left ventricle mass, $|\Gamma_0^{\text{epi}}|$ is the epicardial surface area and where we assumed that $\mathbf{N} \simeq \mathbf{e}_\rho$ on the epicardium. By dimensional analysis, we assume that the ventricle volume and radius are linked by a relationship of the type of $V_{\text{LV}}(t) = \alpha r^3(t)$, for some constant α. For a half-spherical cavity, e.g., we have $\alpha = \frac{2}{3}\pi$. It follows

$$\begin{aligned}
\dot{r}^2(t) &= \frac{1}{9}\alpha^{-\frac{2}{3}} V^{-\frac{4}{3}}(t)\dot{V}^2(t)\\
\frac{d}{dt}\left(\dot{r}^2(t)\right) &= \frac{2}{9}\alpha^{-\frac{2}{3}} V^{-\frac{4}{3}}(t)\left[\ddot{V}(t) - \frac{2}{9}V^{-1}(t)\dot{V}^2(t)\right]\dot{V}(t) \simeq \frac{2}{9}\alpha^{-\frac{2}{3}} V^{-\frac{4}{3}}(t)\ddot{V}(t)\dot{V}(t)
\end{aligned} \tag{46}$$

where we have neglected the term $\dot{V}^2(t)$, under the hypothesis of small velocities.

Concerning the active force power term Π^{act} we notice that, thanks to the identity (see [45])

$$\frac{\mathbf{F}\mathbf{f}_0\otimes\mathbf{f}_0}{\sqrt{\mathcal{I}_{4f}}} = \frac{\partial \lambda}{\partial \mathbf{F}},$$

and assuming an homogeneous active tension and fibers elongation, we have

$$\Pi^{\text{act}}(t) = -\int_{\Omega_0} T_{\text{a}}\, \dot{\lambda}\, d\mathbf{x} \simeq -|\Omega_0|\, T_{\text{a}}(t)\, \dot{\lambda}(t), \tag{47}$$

where $|\Omega_0|$ denotes the volume of the reference domain. Finally, we need to link the fibers elongation λ to the state variable V. We thus assume that $\lambda = \psi(V)$, for some increasing function ψ.

By replacing Eqs. (45)–(47) into Eq. (44), we get

$$\begin{aligned}
&\frac{1}{9} M_{\text{LV}}\, \alpha^{-\frac{2}{3}} V^{-\frac{4}{3}}(t)\ddot{V}(t)\dot{V}(t) + p_{\text{pass}}(V(t))\dot{V}(t) + |\Omega_0|\, T_{\text{a}}(t)\, \psi'(V(t))\dot{V}(t)\\
&\qquad + \frac{1}{9} C_\perp^{\text{epi}} |\Gamma_0^{\text{epi}}| \alpha^{-\frac{2}{3}} V^{-\frac{4}{3}}(t)\dot{V}^2(t) - p(t)\dot{V}(t) = 0,
\end{aligned}$$

which entails

$$M(V)\ddot{V}(t) + C(V)\dot{V}(t) + p_{\text{pass}}(V(t)) + A(V)T_{\text{a}}(t) = p(t),$$

having defined

$$M(V) = \frac{1}{9}M_{\text{LV}}\,\alpha^{-\frac{2}{3}}V^{-\frac{4}{3}}(t), \quad C(V) = \frac{1}{9}C_{\perp}^{\text{epi}}|\Gamma_0^{\text{epi}}|\alpha^{-\frac{2}{3}}V^{-\frac{4}{3}}(t), \quad A(V) = |\Omega_0|\,\psi'(V(t))$$

as the equivalent mass, viscosity and active stress factor. Finally, for simplicity we assume the factors M, C and A as constants by setting $M = M(\overline{V})$, $C = C(\overline{V})$ and $A = A(\overline{V})$, for a reference volume $\overline{V}$. The minimal model thus reads:

$$M\,\ddot{V}(t) + C\,\dot{V}(t) + p_{\text{pass}}(V(t)) + A\,T_{\text{a}}(t) = p(t). \tag{48}$$

To provide realistic values of the coefficients entering in Eq. (48), we consider the 3D electromechanical model, based on the Zygote heart [53], described in Sec. 5.2.1. Specifically, we set $|\Omega_0| = 100\,\text{mL}$, $|\Gamma_0^{\text{epi}}| = 140\,\text{cm}^2$, $M_{\text{LV}} = 0.1\,\text{kg}$ and $C_{\perp}^{\text{epi}} = 2\cdot 10^4\,\text{Pa}\,\text{s}\,\text{m}^{-1}$. To link the chamber radius and its volume, we assume a half-sphere approximation ($\alpha = \frac{2}{3}\pi$). From simulation data, we estimate the derivative of ψ as $\psi' = 3.5\cdot 10^{-3}\,\text{mL}^{-1}$. To define p_{pass}, we fit the end-diastolic pressure-volume relationship through the Klotz's curve [26] of Eq. (42). Finally, to compute the coefficients we set $\overline{V} = 120\,\text{mL}$. The resulting coefficients are reported in Tab. 1.

Appendix B The effect of active stress on numerical stability

We here provide details on the discussion of Sec. 3.3.3, regarding the role played by active stress in the stability analysis of Sec. 3. As a minimal model of active force generation, we consider the generalized Huxley model of [40], that reads

$$\begin{cases} \dot{K}_{\text{a}}(t) = -r\,K_{\text{a}}(t) + \mu_K P(t), & t > 0, \\ \dot{T}_{\text{a}}(t) = -r\,T_{\text{a}}(t) + \mu_T P(t) + \dot{\lambda}(t)\,K_{\text{a}}(t), & t > 0, \\ K_{\text{a}}(0) = K_{\text{a},0}, \quad T_{\text{a}}(0) = T_{\text{a},0}, \end{cases} \tag{49}$$

where r, μ_K and μ_T are suitable constants and $P(t)$ represents the fraction of permissive regulatory units at time t. The so-called permissivity $P(t)$ is in fact the chemical input of the model. Specifically, we have $P(t) = 0$ when the tissue is relaxed, $P(t) > 0$ when activated. As shown in [40], model (49) exhibits the main experimental features of force generation in sarcomeres and can be regarded as a linearization of more complex models. To link the microscopic to the macroscopic level, coherently with the derivation Appendix A, we set $\lambda(t) = \psi(V(t))$. Let us consider the ND scheme, that reads

$$\begin{cases} M\dfrac{V_{\mathcal{S}}^{(k+1)} - 2V_{\mathcal{S}}^{(k)} + V_{\mathcal{S}}^{(k-1)}}{\Delta t^2} + C\dfrac{V_{\mathcal{S}}^{(k+1)} - V_{\mathcal{S}}^{(k)}}{\Delta t} + p_{\text{pass}}(V_{\mathcal{S}}^{(k+1)}) + A\,T_{\text{a}}^{(k+1)} = p^{(k+1)} & k = 0,1,\dots \\ \dfrac{K_{\text{a}}^{(k+1)} - K_{\text{a}}^{(k)}}{\Delta t} = -r\,K_{\text{a}}^{(k+1)} + \mu_K P(t_{k+1}), & k = 0,1,\dots \\ \dfrac{T_{\text{a}}^{(k+1)} - T_{\text{a}}^{(k)}}{\Delta t} = -r\,T_{\text{a}}^{(k+1)} + \mu_T P(t_{k+1}) + \dfrac{\psi(V_{\mathcal{S}}^{(k+1)}) - \psi(V_{\mathcal{S}}^{(k)})}{\Delta t}\,K_{\text{a}}^{(k+1)}, & k = 0,1,\dots \\ V_{\mathcal{S}}^{(k+1)} = V_{\mathcal{F}}^{(k)} & k = 0,1,\dots \\ \dfrac{V_{\mathcal{F}}^{(k+1)} - V_{\mathcal{F}}^{(k)}}{\Delta t} = Q_{\text{valve}}(p_{\text{ext}}(t_{k+1}) - p^{(k+1)}) \quad k = 0,1,\dots \end{cases} \tag{50}$$

The updated active stress then reads

$$T_{\text{a}}^{(k+1)} = \frac{1}{1 + r\Delta t}\left[T_{\text{a}}^{(k)} + K_{\text{a}}^{(k+1)}\left(\psi(V_{\mathcal{S}}^{(k+1)}) - \psi(V_{\mathcal{S}}^{(k)})\right) + \Delta t\mu_T P(t_{k+1})\right]. \tag{51}$$

Thus, for $\Delta t \to 0^+$

$$T_{\mathrm{a}}^{(k+1)} \approx T_{\mathrm{a}}^{(k)} + K_{\mathrm{a}}^{(k+1)} \left(\psi(V_{\mathcal{S}}^{(k+1)}) - \psi(V_{\mathcal{S}}^{(k)}) \right) \tag{52}$$

which entails (since $K_{\mathrm{a}}^{(k)}$ varies slowly) that

$$T_{\mathrm{a}}^{(k+1)} \approx \overline{T}_{\mathrm{a}} + K_{\mathrm{a}}^{(k+1)} \psi(V_{\mathcal{S}}^{(k+1)}), \tag{53}$$

Replacing Eq. (53) into Eq. (50), we get:

$$M \frac{V_{\mathcal{S}}^{(k+1)} - 2V_{\mathcal{S}}^{(k)} + V_{\mathcal{S}}^{(k-1)}}{\Delta t^2} + C \frac{V_{\mathcal{S}}^{(k+1)} - V_{\mathcal{S}}^{(k)}}{\Delta t} + p_{\mathrm{pass}}(V_{\mathcal{S}}^{(k+1)}) + A\, K_{\mathrm{a}}^{(k+1)} \psi(V_{\mathcal{S}}^{(k+1)}) + A\, \overline{T}_{\mathrm{a}} = p^{(k+1)} \tag{54}$$

Therefore, we formally recover the case of prescribed active stress (see Eq. (15)), provided that we replace the purely passive pressure function $p_{\mathrm{pass}}(V_{\mathcal{S}})$ with

$$p_{\mathrm{pass+act}}(V_{\mathcal{S}}) = p_{\mathrm{pass}}(V_{\mathcal{S}}) + A\, K_{\mathrm{a}} \psi(V_{\mathcal{S}}). \tag{55}$$

The first term of Eq. (55) accounts for the passive elastance, while the second one accounts for the active elastance, due to microscale crossbridge links. In conclusion, for $\Delta t \to 0^+$, the stability analysis of Sec. 3.3 is still valid, provided that we redefine the elastance as $E = E_{\mathrm{pass}} + E_{\mathrm{act}}$, where

$$E_{\mathrm{pass}}(V_{\mathcal{S}}) = p'_{\mathrm{pass}}(V_{\mathcal{S}}); \qquad E_{\mathrm{act}}(V_{\mathcal{S}}) = A\, K_{\mathrm{a}} \psi'(V_{\mathcal{S}}). \tag{56}$$

By using the parameters of the original model (see [40]), we get $E_{\mathrm{act}} = 36\,\mathrm{mmHg\,mL^{-1}}$.

We now check whether the two additional eigenvalues associated with the dynamics of K_{a} and T_{a} can introduce instabilities in the numerical solution or not. From the second equation, it follows

$$K_{\mathrm{a}}^{(k+1)} = \frac{1}{1 + r\Delta t} \left[K_{\mathrm{a}}^{(k)} + \Delta t \mu_K P(t_{k+1}) \right]. \tag{57}$$

Thus, the active stiffness dynamics is associated with the eigenvalue

$$\mu = (1 + r\Delta t)^{-1} < 1, \tag{58}$$

that cannot be responsible of numerical instabilities, being strictly lower than one.

To study the eigenvalue associated with the dynamics of T_{a}, instead, we consider the following approximate equation, obtained by neglecting high-order effects in the mechanics equilibrium and by subtracting the equation for two consecutive time steps:

$$\begin{aligned} p^{(k+1)} - p^{(k)} &\approx \left(p_{\mathrm{pass}}(V_{\mathcal{S}}^{(k+1)}) - p_{\mathrm{pass}}(V_{\mathcal{S}}^{(k)}) \right) + A \left(T_{\mathrm{a}}^{(k+1)} - T_{\mathrm{a}}^{(k)} \right) \\ &\approx E_{\mathrm{pass}}(V_{\mathcal{S}}^{(k+1)}) \left(V_{\mathcal{S}}^{(k+1)} - V_{\mathcal{S}}^{(k)} \right) + A \left(T_{\mathrm{a}}^{(k+1)} - T_{\mathrm{a}}^{(k)} \right) \\ &\approx \frac{E_{\mathrm{pass}}(V_{\mathcal{S}}^{(k+1)})}{\psi'(V_{\mathcal{S}}^{(k+1)})} \left(\psi(V_{\mathcal{S}}^{(k+1)}) - \psi(V_{\mathcal{S}}^{(k)}) \right) + A \left(T_{\mathrm{a}}^{(k+1)} - T_{\mathrm{a}}^{(k)} \right). \end{aligned} \tag{59}$$

Therefore, replacing (59) into Eq. (50), we have

$$\begin{aligned} (1 + r\Delta t)\, T_{\mathrm{a}}^{(k+1)} &= T_{\mathrm{a}}^{(k)} + K_{\mathrm{a}}^{(k+1)} \left(\psi(V_{\mathcal{S}}^{(k+1)}) - \psi(V_{\mathcal{S}}^{(k)}) \right) + \Delta t \mu_T P(t_{k+1}) \\ &\approx T_{\mathrm{a}}^{(k)} + \frac{K_{\mathrm{a}}^{(k+1)} \psi'(V_{\mathcal{S}}^{(k+1)})}{E_{\mathrm{pass}}(V_{\mathcal{S}}^{(k+1)})} \left(\left(p^{(k+1)} - p^{(k)} \right) - A \left(T_{\mathrm{a}}^{(k+1)} - T_{\mathrm{a}}^{(k)} \right) \right) \\ &\quad + \Delta t \mu_T P(t_{k+1}), \end{aligned} \tag{60}$$

which entails that the eigenvalue associated with the dynamics of T_{a} is approximated by

$$\mu = \frac{1 + \frac{E_{\mathrm{act}}}{E_{\mathrm{pass}}}}{1 + r\Delta t + \frac{E_{\mathrm{act}}}{E_{\mathrm{pass}}}} < 1, \tag{61}$$

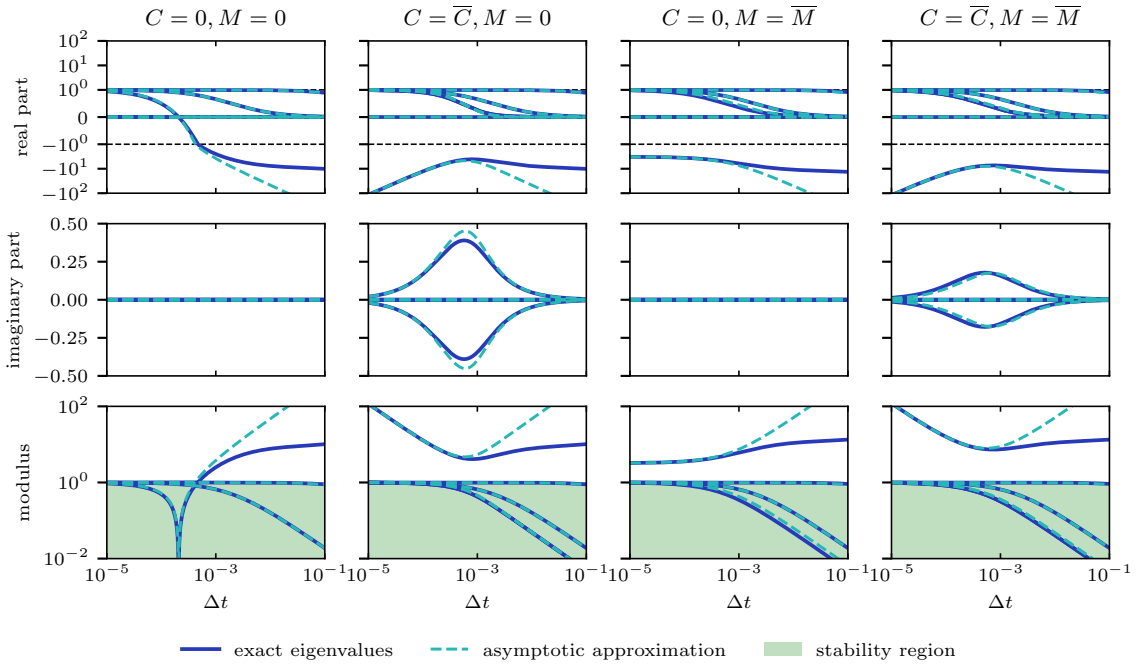

Figure 17: Eigenvalues of the Jacobian matrix $-\mathbf{A}^{-1}\mathbf{B}$ for the ND scheme in the open valve case: comparison of the exact eigenvalues and their approximation obtained through the asymptotic analysis of Appendix B.

which cannot lead to numerical instabilities either.

To validate the results of the asymptotic analysis of the current appendix, we numerically compute the eigenvalues of the Jacobian matrix $-\mathbf{A}^{-1}\mathbf{B}$ associated with the ND scheme when the model $\mathcal{F}$–$\mathcal{S}$ is coupled with the activation model (49) (that is scheme (50)) under different conditions (quasi-static case, with viscosity, inertia or both) and for different values of Δt. Then, we compare the results with the eigenvalues obtained when the ND scheme is applied to the $\mathcal{F}$–$\mathcal{S}$ alone (that is scheme (15)), with an increased elastance ($E = E_{\text{pass}} + E_{\text{act}}$). To the latter set eigenvalues, we also append the estimated eigenvalues of Eqs. (58) and (61). The results, shown in Fig. 17, show that, as expected, for small values of Δt the approximation is very accurate. Moreover, the eigenvalues obtained through the asymptotic approximation provide an accurate estimate of the stability thresholds.

Appendix C Algorithm for the resolution of the structure mechanics substep of the ND-stab scheme

We present an algorithm for the numerical resolution of the nonlinear system of equations arising from the structure mechanics substep of the ND-stab scheme of Eq. (41). To ease the notation, we write the nonlinear system at hand as

$$\begin{cases} \mathbf{r}_{\mathbf{d}}^{(k)}(\mathbf{d}^{(k+1)}, \mathbf{p}^{(k+1)}) = \mathbf{0}, \\ \mathbf{r}_{\mathbf{p}}^{(k)}(\mathbf{d}^{(k+1)}, \mathbf{p}^{(k+1)}) = \mathbf{0}, \end{cases} \tag{62}$$

having defined the residuals

$$\mathbf{r}_{\mathbf{d}}^{(k)}(\mathbf{d}^{(k+1)}, \mathbf{p}^{(k+1)}) = \mathcal{L}\left(\frac{\mathbf{d}^{(k+1)} - 2\mathbf{d}^{(k)} + \mathbf{d}^{(k-1)}}{\Delta t^2}, \frac{\mathbf{d}^{(k+1)} - \mathbf{d}^{(k)}}{\Delta t}, \mathbf{d}^{(k+1)}, \mathbf{p}^{(k+1)}, t_{k+1}\right),$$
$$\mathbf{r}_{\mathbf{p}}^{(k)}(\mathbf{d}^{(k+1)}, \mathbf{p}^{(k+1)}) = \mathbf{V}_{\mathcal{S}}(\mathbf{d}^{(k+1)}) - \mathbf{V}_{\mathcal{F}}(\mathbf{c}^{(k)}) - \Delta t\, \mathbf{Q}_{\text{stab}}(\mathbf{p}^{(k+1)}, \mathbf{c}^{(k)}, t_{k+1}).$$

We solve the nonlinear system (62) by means the Newton method. Specifically, to update the state variables $(\mathbf{d}^{(k)}, \mathbf{p}^{(k)})$ from iteration k to $k+1$, we set $\mathbf{d}^0 = \mathbf{d}^{(k)}$, $\mathbf{p}^0 = \mathbf{p}^{(k)}$ and then we iteratively update according to $\mathbf{d}^{j+1} = \mathbf{d}^j + \Delta\mathbf{d}^j$, $\mathbf{p}^{j+1} = \mathbf{p}^j + \Delta\mathbf{d}^j$, where the increments $\Delta\mathbf{d}^j$ and $\Delta\mathbf{d}^j$ are solution of the linear system

$$\begin{pmatrix} \mathbf{J}^j_{\mathbf{dd}} & \mathbf{J}^j_{\mathbf{dp}} \\ \mathbf{J}^j_{\mathbf{pd}} & \mathbf{J}^j_{\mathbf{pp}} \end{pmatrix} \begin{pmatrix} \Delta\mathbf{d}^j \\ \Delta\mathbf{p}^j \end{pmatrix} = - \begin{pmatrix} \mathbf{r}^{(k)}_{\mathbf{d}}(\mathbf{d}^j, \mathbf{p}^j) \\ \mathbf{r}^{(k)}_{\mathbf{p}}(\mathbf{d}^j, \mathbf{p}^j) \end{pmatrix}. \tag{63}$$

Finally, we set $\mathbf{d}^{(k+1)} = \mathbf{d}^j$, $\mathbf{p}^{(k+1)} = \mathbf{p}^j$ where j is the Newton iteration after a suitable convergence criterion is attained.

Concerning the numerical solution of the linear system (63), we adopt a Schur complement reduction, as proposed in [43, 44]. We notice that, denoting by N the number of cavities in the mechanical model, we can split the matrices and vectors as

$$\mathbf{J}^j_{\mathbf{dp}} = \begin{pmatrix} | & & | \\ \mathbf{j}_{\mathbf{d}1} & \cdots & \mathbf{j}_{\mathbf{d}N} \\ | & & | \end{pmatrix}, \qquad \Delta\mathbf{p}^j = \begin{pmatrix} \Delta p_1 \\ \vdots \\ \Delta p_N \end{pmatrix},$$

$$\mathbf{J}^j_{\mathbf{pd}} = \begin{pmatrix} — & \mathbf{j}^T_{1\mathbf{d}} & — \\ & \vdots & \\ — & \mathbf{j}^T_{N\mathbf{d}} & — \end{pmatrix}, \qquad \mathbf{r}^{(k)}_{\mathbf{p}}(\mathbf{d}^j, \mathbf{p}^j) = \begin{pmatrix} \mathbf{r}_1 \\ \vdots \\ \mathbf{r}_N \end{pmatrix}.$$

At each Newton iteration we first solve the following $N+1$ linear system associated with the Jacobian matrix of the structure mechanics problem:

$$\mathbf{J}^j_{\mathbf{dd}}\mathbf{w} = \mathbf{r}^{(k)}_{\mathbf{d}}(\mathbf{d}^j, \mathbf{p}^j), \qquad \mathbf{J}^j_{\mathbf{dd}}\mathbf{w}_i = \mathbf{j}_{\mathbf{d}i} \quad \text{for } i = 1, \ldots, N.$$

Then, we recover the pressure increments by solving the $N \times N$ linear system (we recall that $N \leq 4$):

$$\left[\mathbf{J}^j_{\mathbf{pp}} - \begin{pmatrix} — & \mathbf{j}^T_{1\mathbf{d}} & — \\ & \vdots & \\ — & \mathbf{j}^T_{N\mathbf{d}} & — \end{pmatrix} \begin{pmatrix} | & & | \\ \mathbf{w}_1 & \cdots & \mathbf{w}_N \\ | & & | \end{pmatrix} \right] \Delta\mathbf{p}^j = \begin{pmatrix} \mathbf{r}_1 - \mathbf{j}_{1\mathbf{d}} \cdot \mathbf{w} \\ \vdots \\ \mathbf{r}_N - \mathbf{j}_{N\mathbf{d}} \cdot \mathbf{w}. \end{pmatrix}$$

Finally, the displacement increment is computed as:

$$\Delta\mathbf{d}^j = -\mathbf{w} - \sum_{i=2}^{N} \mathbf{w}_i \Delta p_i.$$

References

[1] T. Arts, T. Delhaas, P. Bovendeerd, X. Verbeek, and F. W. Prinzen. "Adaptation to mechanical load determines shape and properties of heart and circulation: the CircAdapt model". In: *American Journal of Physiology-Heart and Circulatory Physiology* 288.4 (2005), H1943–H1954.

[2] M. Astorino and C. Grandmont. "Convergence analysis of a projection semi-implicit coupling scheme for fluid–structure interaction problems". In: *Numerische Mathematik* 116.4 (2010), pp. 721–767.

[3] C. M. Augustin, M. A. Gsell, E. Karabelas, E. Willemen, F. W. Prinzen, J. Lumens, E. J. Vigmond, and G. Plank. "A computationally efficient physiologically comprehensive 3D–0D closed-loop model of the heart and circulation". In: *Computer Methods in Applied Mechanics and Engineering* 386 (2021), p. 114092.

[4] S. Badia, F. Nobile, and C. Vergara. "Fluid–structure partitioned procedures based on Robin transmission conditions". In: *Journal of Computational Physics* 227.14 (2008), pp. 7027–7051.

[5] Y. Bao, A. Donev, and B. E. Griffith. "An immersed boundary method with divergence-free velocity interpolation". In: *Journal of Computational Physics* 347 (2017), pp. 183–206.

[6] J. D. Bayer, R. C. Blake, G. Plank, and N. A. Trayanova. "A novel rule-based algorithm for assigning myocardial fiber orientation to computational heart models". In: *Annals of Biomedical Engineering* 40.10 (2012), pp. 2243–2254.

[7] P. J. Blanco and R. A. Feijóo. "A 3D-1D-0D Computational Model for the Entire Cardiovascular System". In: *Computational Mechanics* 24 (2010), pp. 5887–5911.

[8] P. Causin, J.-F. Gerbeau, and F. Nobile. "Added-mass effect in the design of partitioned algorithms for fluid–structure problems". In: *Computer methods in applied mechanics and engineering* 194.42-44 (2005), pp. 4506–4527.

[9] P. Colli Franzone, L. Pavarino, and S. Scacchi. *Mathematical cardiac electrophysiology*. Vol. 13. Springer, 2014.

[10] L. Dedè, A. Quarteroni, and F. Regazzoni. "Mathematical and numerical models for the cardiac electromechanical function". In: *Atti della Accademia Nazionale dei Lincei, Classe di Scienze Fisiche, Matematiche e Naturali. Rendiconti Lincei - Matematica e Applicazioni* 32.2 (2021), pp. 233–272.

[11] S. Deparis, M. A. Fernández, and L. Formaggia. "Acceleration of a fixed point algorithm for fluid-structure interaction using transpiration conditions". In: *ESAIM: Mathematical Modelling and Numerical Analysis* 37.4 (2003), pp. 601–616.

[12] M. Fedele and A. Quarteroni. "Polygonal surface processing and mesh generation tools for the numerical simulation of the cardiac function". In: *Int J Numer Meth Biomed Engng* (2021).

[13] M. A. Fernández. "Incremental displacement-correction schemes for incompressible fluid-structure interaction". In: *Numerische Mathematik* 123.1 (2013), pp. 21–65.

[14] M. A. Fernández and J. Mullaert. "Convergence and error analysis for a class of splitting schemes in incompressible fluid–structure interaction". In: *IMA Journal of Numerical Analysis* 36.4 (2016), pp. 1748–1782.

[15] L. Formaggia, A. Moura, and F. Nobile. "On the stability of the coupling of 3D and 1D fluid-structure interaction models for blood flow simulations". In: *ESAIM: Mathematical Modelling and Numerical Analysis* 41.4 (2007), pp. 743–769.

[16] C. Förster, W. A. Wall, and E. Ramm. "Artificial added mass instabilities in sequential staggered coupling of nonlinear structures and incompressible viscous flows". In: *Computer methods in applied mechanics and engineering* 196.7 (2007), pp. 1278–1293.

[17] L. Gerardo-Giorda, F. Nobile, and C. Vergara. "Analysis and optimization of Robin–Robin partitioned procedures in fluid-structure interaction problems". In: *SIAM Journal on Numerical Analysis* 48.6 (2010), pp. 2091–2116.

[18] A. Gerbi. "Numerical Approximation of Cardiac Electro-fluid-mechanical Models: Coupling Strategies for Large-scale Simulation". PhD thesis. Ecole Polytechnique Fédérale de Lausanne, 2018.

[19] A. Gerbi, L. Dedè, and A. Quarteroni. "A monolithic algorithm for the simulation of cardiac electromechanics in the human left ventricle". In: *Mathematics in Engineering* 1.1 (2018), pp. 1–37.

[20] B. E. Griffith and N. A. Patankar. "Immersed methods for fluid-structure interaction". In: *Annual Review of Fluid Mechanics* 52 (2020), pp. 421–448.

[21] M. E. Gurtin. *An introduction to continuum mechanics*. Academic press, 1982.

[22] A. Hill. "The heat of shortening and the dynamic constants of muscle". In: *Proceedings of the Royal Society of London B: Biological Sciences* 126.843 (1938), pp. 136–195.

[23] M. Hirschvogel, M. Bassilious, L. Jagschies, and et al. "A monolithic 3D-0D coupled closed-loop model of the heart and the vascular system: Experiment-based parameter estimation for patient-specific cardiac mechanics". In: *International Journal for Numerical Methods in Biomedical Engineering* 33.8 (2017), e2842.

[24] G. Hou, J. Wang, and A. Layton. "Numerical methods for fluid-structure interaction—a review". In: *Communications in Computational Physics* 12.2 (2012), pp. 337–377.

[25] R. C. Kerckhoffs, M. L. Neal, Q. Gu, J. B. Bassingthwaighte, J. H. Omens, and A. D. McCulloch. "Coupling of a 3D finite element model of cardiac ventricular mechanics to lumped systems models of the systemic and pulmonic circulation". In: *Annals of Biomedical Engineering* 35.1 (2007), pp. 1–18.

[26] S. Klotz, I. Hay, M. L. Dickstein, G.-H. Yi, J. Wang, M. S. Maurer, D. A. Kass, and D. Burkhoff. "Single-beat estimation of end-diastolic pressure-volume relationship: a novel method with potential for noninvasive application". In: *American Journal of Physiology-Heart and Circulatory Physiology* 291.1 (2006), H403–H412.

[27] S. G. Krantz and H. R. Parks. *The implicit function theorem: history, theory, and applications*. Springer Science & Business Media, 2012.

[28] U. Küttler and W. A. Wall. "Fixed-point fluid–structure interaction solvers with dynamic relaxation". In: *Computational mechanics* 43.1 (2008), pp. 61–72.

[29] S. Land, S. Park-Holohan, N. Smith, C. dos Remedios, J. Kentish, and S. Niederer. "A model of cardiac contraction based on novel measurements of tension development in human cardiomyocytes". In: *Journal of Molecular and Cellular Cardiology* 106 (2017), pp. 68–83.

[30] S. Land, S. A. Niederer, J. M. Aronsen, E. K. Espe, L. Zhang, W. E. Louch, I. Sjaastad, O. M. Sejersted, and N. P. Smith. "An analysis of deformation-dependent electromechanical coupling in the mouse heart". In: *The Journal of Physiology* 590.18 (2012), pp. 4553–4569.

[31] E. Lefrançois and J.-P. Boufflet. "An introduction to fluid-structure interaction: application to the piston problem". In: *SIAM review* 52.4 (2010), pp. 747–767.

[32] F Levrero-Florencio, F Margara, E Zacur, A Bueno-Orovio, Z. Wang, A Santiago, J Aguado-Sierra, G Houzeaux, V Grau, D Kay, et al. "Sensitivity analysis of a strongly-coupled human-based electromechanical cardiac model: Effect of mechanical parameters on physiologically relevant biomarkers". In: *Computer Methods in Applied Mechanics and Engineering* 361 (2020), p. 112762.

[33] S. A. Niederer, P. J. Hunter, and N. P. Smith. "A quantitative analysis of cardiac myocyte relaxation: a simulation study". In: *Biophysical Journal* 90.5 (2006), pp. 1697–1722.

[34] R. W. Ogden. *Non-linear elastic deformations*. Courier Corporation, 1997.

[35] R. Piersanti, F. Regazzoni, M. Salvador, A. F. Corno, L. Dede, C. Vergara, and A. Quarteroni. "3D-0D closed-loop model for the simulation of cardiac biventricular electromechanics". In: *Computer Methods in Applied Mechanics and Engineering* (accepted) (2021).

[36] A. Quarteroni, R. Sacco, and F. Saleri. *Numerical mathematics*. Vol. 37. Springer Science & Business Media, 2010.

[37] A. Quarteroni, L. Dede', A. Manzoni, and C. Vergara. *Mathematical modelling of the human cardiovascular system: data, numerical approximation, clinical applications*. Cambridge Monographs on Applied and Computational Mathematics. Cambridge University Press, 2019.

[38] A. Quarteroni and A. Valli. *Domain decomposition methods for partial differential equations*. BOOK. Oxford University Press, 1999.

[39] A. Quarteroni and A. Valli. *Numerical approximation of partial differential equations*. Vol. 23. Springer Science & Business Media, 2008.

[40] F. Regazzoni, L. Dedè, and A. Quarteroni. "Active force generation in cardiac muscle cells: mathematical modeling and numerical simulation of the actin-myosin interaction". In: *Vietnam Journal of Mathematics* (2020), pp. 1–32.

[41] F. Regazzoni, L. Dedè, and A. Quarteroni. "Biophysically detailed mathematical models of multiscale cardiac active mechanics". In: *PLOS Computational Biology* 16.10 (2020), e1008294.

[42] F. Regazzoni, L. Dedè, and A. Quarteroni. "Machine learning of multiscale active force generation models for the efficient simulation of cardiac electromechanics". In: *Computer Methods in Applied Mechanics and Engineering* 370 (2020), p. 113268.

[43] F. Regazzoni, M. Salvador, P. C. Africa, M Fedele, L. Dede', and A. Quarteroni. "A cardiac electromechanics model coupled with a lumped parameters model for closed-loop blood circulation. Part I: model derivation". In: *arXiv preprint arXiv:2011.15040* (2020).

[44] F. Regazzoni. "Mathematical modeling and Machine Learning for the numerical simulation of cardiac electromechanics". PhD thesis. Politecnico di Milano, 2020.

[45] F. Regazzoni and A. Quarteroni. "An oscillation-free fully partitioned scheme for the numerical modeling of cardiac active mechanics". In: *Computer Methods in Applied Mechanics and Engineering* 373 (2021), p. 113506.

[46] J. Rice, F. Wang, D. Bers, and P. de Tombe. "Approximate model of cooperative activation and crossbridge cycling in cardiac muscle using ordinary differential equations". In: *Biophysical Journal* 95.5 (2008), pp. 2368–2390.

[47] J. Rice, R. Winslow, and W. Hunter. "Comparison of putative cooperative mechanisms in cardiac muscle: length dependence and dynamic responses". In: *American Journal of Physiology-Heart and Circulatory Physiology* 276.5 (1999), H1734–H1754.

[48] P. L. Tallec and S. Mani. "Numerical analysis of a linearised fluid-structure interaction problem". In: *Numerische Mathematik* 87.2 (2000), pp. 317–354.

[49] K. H. Ten Tusscher and A. V. Panfilov. "Alternans and spiral breakup in a human ventricular tissue model". In: *American Journal of Physiology-Heart and Circulatory Physiology* 291.3 (2006), H1088–H1100.

[50] A. Toselli and O. Widlund. *Domain decomposition methods-algorithms and theory*. Vol. 34. Springer Science & Business Media, 2004.

[51] T. P. Usyk, I. J. LeGrice, and A. D. McCulloch. "Computational model of three-dimensional cardiac electromechanics". In: *Computing and Visualization in Science* 4.4 (2002), pp. 249–257.

[52] T. Washio, K. Yoneda, J. Okada, T. Kariya, S. Sugiura, and T. Hisada. "Ventricular fiber optimization utilizing the branching structure". In: *International Journal for Numerical Methods in Biomedical Engineering* (2015), e02753.

[53] *Zygote 3D models*. 2019. URL: `https://www.zygote.com/`.

MOX Technical Reports, last issues

Dipartimento di Matematica
Politecnico di Milano, Via Bonardi 9 - 20133 Milano (Italy)

15/2022 G. Ciaramella, T. Vanzan
Spectral coarse spaces for the substructured parallel Schwarz method

16/2022 G. Ciaramella, T. Vanzan
Substructured Two-grid and Multi-grid Domain Decomposition Methods

14/2022 Zappon, E.; Manzoni, A.; Quarteroni A.
Efficient and certified solution of parametrized one-way coupled problems through DEIM-based data projection across non-conforming interfaces

13/2022 Grasselli, M.; Parolini, N.; Poiatti, A.; Verani, M.
Non-isothermal non-Newtonian fluids: the stationary case

12/2022 Antonietti, P.F.; Dassi, F.; Manuzzi, E.
Machine Learning based refinement strategies for polyhedral grids with applications to Virtual Element and polyhedral Discontinuous Galerkin methods

11/2022 Sampaoli, S.; Agosti, A.; Pozzi, G.; Ciarletta,P.
A toy model of misfolded protein aggregation and neural damage propagation in neudegenerative diseases

09/2022 Corti, M.; Zingaro, A.; Dede', L.; Quarteroni, A.
Impact of Atrial Fibrillation on Left Atrium Haemodynamics: A Computational Fluid Dynamics Study

10/2022 Fresca, S.; Manzoni, A.
Real-time simulation of parameter-dependent fluid flows through deep learning-based reduced order models

08/2022 Gobat, G.; Opreni, A.; Fresca, S.; Manzoni, A.; Frangi, A.
Reduced order modeling of nonlinear microstructures through Proper Orthogonal Decomposition

07/2022 Sinigaglia, C.; Quadrelli, D.E.; Manzoni, A.; Braghin, F.
Fast active thermal cloaking through PDE-constrained optimization and reduced-order modeling